

# Fiber numerical aperture Characterization for the single fiber reflectance technique

Fiber numerical aperture dependence on wavelength  
and bending



Bachelor of engineering thesis  
Applied Physics

Author: G.B. Loozen  
Student number: 07000987  
Mentor: dr. A.J. Lock  
Supervisor: dr. A. Amelink  
Date: 01-06-2012

**THE HAGUE**  
UNIVERSITY OF  
APPLIED SCIENCES



**Erasmus MC**  
University Medical Center Rotterdam  
*Erasmus*

# Abstract

---

Single Fiber Reflectance spectroscopy (SFR) can be used to determine tissue optical properties such as scattering and absorption. The SFR technique employs a semi-empirical modal, which contains a parameter that is dependent on the fiber numerical aperture,  $NA$ . However, the  $NA$  is a wavelength dependent quantity and also changes when the fiber is bent. In order to account for the error in SFR measurements caused by these changes, the  $NA$  will have to be characterized. This study will focus on investigating the  $NA$  dependence on wavelength and bending.

Firstly, a far field profile scan method was developed in order to determine the  $NA$  dependence on wavelength and bending. Various fiber output profiles were collected and the  $NA$  was defined as the angular value in which the profile intensity has dropped to 5% of the maximum profile intensity. Results show a disturbance of the profile scans of light that exits the fiber at angles that are larger than the 5% angle, which is caused by light that is coupled into the cladding at the fiber proximal end. This effect caused an increase in  $NA$  of a factor of two. This problem was accounted for by placing a pinhole at the fiber proximal end to prevent light from being coupled into the fiber. The effect of different pinholes at the proximal end of fibers of different diameters was investigated. Another problem where the low signals acquired when measuring at the distances defined to be in the far field region. This motivated the investigation of the variation in  $NA$  when measuring at distances that are smaller than the far field distance. These measurements were compared with a measurement performed on a 200  $\mu\text{m}$  fiber placed in the far field region. All results show a  $NA$  varying from 0.23 to 0.22 in a spectral range of 400-900 nm with an uncertainty of 0.02. These results all correspond to the  $NA$  of 0.22 with 0.02 inaccuracy specified by the manufacturer.

Secondly, the  $NA$  was also determined by CCD camera measurements. These measurements also showed promising results. CCD images were also taken of the fiber profile without pinhole at the proximal end to illustrate the effects of cladding modes on the profile.

Lastly, bend measurements were performed on different fibers that showed a monotonically decreasing  $NA$  at large bend radii and a wavelength dependent oscillatory behavior of the  $NA$  at small bend radii. These effects were described qualitatively by means of published results.

# Table of contents

---

Abstract.....	2
Table of contents .....	3
1. Introduction .....	5
2. Light propagation in tissue and the SFR technique .....	7
2.1 Tissue absorption and scattering properties .....	7
2.2 The Single Fiber Reflectance technique.....	10
3. Light propagation in optical fibers .....	12
3.1 Total Internal Reflection and fiber Numerical Aperture.....	12
3.2 Cladding modes.....	15
4. Optical fibers and macrobending.....	19
4.2 Macro bending described geometrically. ....	19
4.2 Wavelength dependent bending loss .....	21
5. Materials and methods .....	24
5.1 Fiber Numerical Aperture measurements .....	24
5.1.1 Measurement method .....	24
5.1.2 Measurement setup.....	25
5.1.3 Measurement Procedure .....	27
5.2 CCD camera measurements.....	28
5.2.1 Measurement method.....	28
5.2.2 Measurement setup.....	28
5.2.3 Measurement procedure.....	29
5.3 Macro bending measurements.....	30
5.3.1 Measurement method .....	30
5.3.2 Measurement setup.....	30
5.3.3 Measurement procedure.....	31
6. Results .....	32
6.1 Fiber NA measurements. ....	32
6.2 CCD camera measurements.....	37
6.3 Fiber bending measurements. ....	41
7. Discussion & Conclusion .....	44
7.1 Discussion.....	44

7.1.1	Fiber NA measurements .....	44
7.1.2	CCD camera measurements.....	45
7.1.3	Fiber bending measurements .....	45
7.2	Conclusion.....	46
Bibliography .....		47
Appendix I: Internship assignment .....		49
Appendix II: Calculations.....		50
II.1	Far field distance calculations.....	50
II.2	Axial alignment error .....	50
II.3	Vertical alignment error.....	53
II.4	Acceptance angle and <b>NA</b> error in CCD camera measurements.....	56
Appendix III: The pinhole setup .....		57

# 1. Introduction

---

A biopsy is a surgical procedure in which a small fraction of tissue is removed for examination. This is most commonly done for the examination of the presence and extent of diseases like cancer. As can be inferred above, a biopsy is an invasive technique which can be painful. What is more, the success of detecting a disease like cancer, for example, relies on an amount of factors. Important factors are:

- The location where the biopsy is taken in relation to size and location of the cancerous region.
- The experience of the physician applying the biopsy, which chiefly determines the detection of the cancer.

These factors and many others make tissue sampling through biopsies very inaccurate. In many cases, patients are called back to repeat the cumbersome biopsy procedure due to insufficient information acquired on the sampled tissue, which is caused by an inaccurate biopsy procedure. In some cases, false conclusions are even drawn on the presence and extent of the cancer. This is why there is a great demand for a more accurate and also noninvasive technique to diagnose tissue for diseases like cancer.

Malignant tissue is characterized by change in tissue structure and physiology. These changes also mean changes in tissue optical properties. The change in tissue optical properties indicates that tissue can also be diagnosed non-invasively with light.

Diagnosis of tissue optical properties is frequently done with reflectance spectroscopy. This is a non-invasive technique in which tissue is illuminated with white light and the fraction of light that is reemitted by the tissue is measured spectrally. The measured light contains information on tissue optical properties, which are related to tissue structure and physiology.

Traditional reflectance spectroscopy setups usually use multiple fibers, in which a number of fibers are used for the transport of light to tissue and a number of fibers are used for the detection of light. However, the use of multiple optical fibers offers certain disadvantages. A main disadvantage is the large probe dimensions that lead to the measurement of bulk tissue optical properties, which makes the setup less suitable for specific clinical procedures like biopsies.

Recently, research has been done by the Center for Optical Diagnosis and Therapy group on Single Fiber Reflectance (SFR) spectroscopy setups which utilize a single fiber for illumination and detection of light, which offers the advantages of small probe dimensions and a simple experimental setup. During research a semi-empirical model has been developed that describes the relation between the reflectance light and tissue optical properties in a single fiber setup. As will be described later on, one parameter of this model is dependent on the fiber Numerical Aperture,  $NA$ .

The  $NA$  is a characteristic property of an optical fiber and is known to vary with the wavelength of light. Additionally, optical fiber the  $NA$  will also vary when a bend is induced on an. The magnitude of this variation is dependent on the bend radius.

Thus, it will be necessary to characterize the  $NA$  dependence on wavelength and bend radius in order to accurately determine tissue optical properties.

This study will focus on investigating the  $NA$  variation with wavelength and bending. In which, the  $NA$  dependence on wavelength will be investigated within a wavelength range of 400-900 nm and the  $NA$  dependence on bend radius will be investigated for different fiber diameters and bend radii.

## 2. Light propagation in tissue and the SFR technique

---

This chapter begins with a brief introduction on light propagation in tissue, in which tissue optical properties are defined. This is done to give a basic understanding on how light propagates in tissue. This understanding is used later on to explain which effect the optical properties have on the detection of light when applying reflectance spectroscopy.

The chapter continues with a description of the single fiber reflectance technique. The factors that affect the amount of light detected are explained, in which importance of knowledge on the fiber Numerical Aperture is brought to attention.

### 2.1 Tissue absorption and scattering properties

When tissue is illuminated by white light, the light penetrates into and is propagated by the tissue. When propagating in tissue, the light is attenuated. The attenuation of light in tissue is caused by two factors, which are:

- Absorption
- Scattering

Components of tissue that cause absorption are referred to as tissue chromophores. Each type of chromophore has a unique absorption spectrum and the amount of absorption of a certain chromophore at a given wavelength is determined by the concentration of the chromophore that is present in tissue.

The concept of absorption caused by tissue chromophores can be described by means of a simplistic model, which considers a chromophore as a sphere with a certain geometrical size [1]. When illuminated by light, this sphere will cast a shadow which can be seen as absorption. The size of the shadow can be described by the following expression,

$$\sigma_a = Q_a A \quad (1)$$

Where:

$\sigma_a$	: Absorption cross section	[mm <sup>2</sup> ]
$Q_a$	: Absorption efficiency	[-]
$A$	: The geometrical cross section of the chromophore	[mm <sup>2</sup> ]

Now consider a sample of tissue that contains a certain amount of chromophores per unit volume. The total absorption cross section per unit volume is given by the following expression,

$$\mu_a = c \sigma_a \quad (2)$$

Where:

$\mu_a$	: The absorption coefficient	[mm <sup>-1</sup> ]
$c$	: The concentration	[mm <sup>-3</sup> ]

The absorption coefficient is expressed in inverse length, and is a proportionality factor for the amount of light that is absorbed after propagating a certain length in tissue with a certain chromophore concentration. This indicates that the amount of light transmitted after propagating a length,  $L$ , in tissue is dependent on  $\mu_a$ . This relation is expressed by the Lambert-Beer law as follows,

$$I_t = I_0 e^{-\mu_a L} \quad (3)$$

Where:

$I_t$	: The transmitted intensity	[–]
$I_0$	: The initial intensity	[–]
$L$	: The photon path length	[mm]

Furthermore,  $\mu_a$  is wavelength dependent, because each chromophore has its own unique absorption spectrum.

Thus, knowledge of the change in spectral shape of light transmitted through a tissue sample, by means of a spectral analysis, indicates the presence of certain tissue chromophores. Knowledge of the amount of light absorbed and the path length traversed can be used to calculate  $\mu_a$ , which can be used to determine the amount of a certain chromophore that is present.

Scattering in tissue is caused by fluctuations in the optical refractive index. This fluctuation is caused by the various cells present in tissue and their intracellular structures which contain various components that cause scattering.

Light scattered in tissue can also be described by the model used above to describe absorption. A scattering component in tissue, which is modeled as a sphere, will redirect incident light and so hinder forward propagation, casting a shadow in the forward direction. The size of this shadow is defined by the following expression,

$$\sigma_s = Q_s A \quad (4)$$

Where:

$\sigma_s$	: The scattering cross section	[mm <sup>2</sup> ]
$Q_s$	: The scattering efficiency	[–]

Now consider a sample of tissue with an amount of scattering components per unit volume. The total scattering cross section per unit volume is defined by the following expression,

$$\mu_s = c \sigma_s \quad (5)$$

Where:

$\mu_s$	: The scattering coefficient	[mm <sup>-1</sup> ]
---------	------------------------------	---------------------

Moreover, when light is scattered, it will be divided into a range of scattering angles, each angle with a different fraction of the initial light intensity. This angular distribution of scattering is defined by the scattering Phase Function,  $PF$ . The average angle in which light is scattered is defined by the following expression,

$$g = \langle \cos \theta \rangle \quad (6)$$

Where:

$g$	: The scattering anisotropy	[-]
$\theta$	: The average scattering angle	[rad]

Each scattering component will have an own distinct scattering phase function, which is mainly caused by the size of the particle. Large scattering components will usually scatter light at low scattering angles (in relation to forward scattering), which gives an anisotropy value closer to unity. Smaller scattering components will usually scatter light at larger angles, which gives an anisotropy value closer to zero. Furthermore, the smaller the scattering component is, the more wavelength dependent the scattering becomes.

The combined effect of the scattering coefficient and the angular dependence of the scattering events is defined by the reduced scattering coefficient and is expressed as follows,

$$\mu'_s = \mu_s \cdot (1 - g) \quad (7)$$

Where:

$\mu'_s$	: The reduced scattering coefficient	[mm <sup>-1</sup> ]
----------	--------------------------------------	---------------------

Knowledge of the scattering properties provides information on the size of the scattering components in tissue and also the amount that is present. Additionally, knowledge of tissue scattering components also determine the path length traversed by light in tissue.

## 2.2 The Single Fiber Reflectance technique

Spectral analysis of light transport in tissue is done by means of reflectance spectroscopy technique. In this technique tissue is illuminated by a white light source and the fraction of light reemitted by the tissue is measured. The measured light, which has been propagated by tissue, contains information of the tissue scattering and absorption properties. Reflectance spectroscopy is usually applied with multiple optical fibers for delivery and collection of light.

Single fiber reflectance spectroscopy is applied with a single optical fiber that is used for both delivery and collection of light. With SFR, local tissue optical properties are measured, in contrast to measurements with multiple fibers where bulk tissue optical properties are measured. This is an advantage because certain clinical applications, such as biopsy procedures, require the measurement of local tissue optical properties. Other advantages are the small dimensions of the fiber which enables incorporation into biopsy needles and a simple measurement setup. A schematic of the SFR measurement setup is illustrated in figure 1.

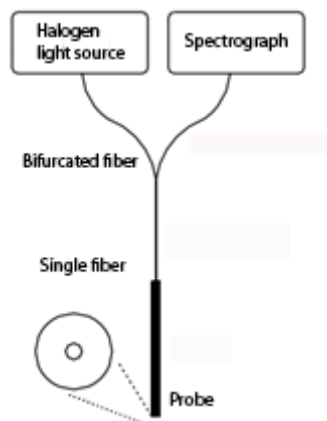


Figure 1: A schematic of the SFR measurement probe. From [2]

As can be seen in figure 1 light from a Halogen lamp light source is coupled to a fiber and is guided via one arm of the bifurcated fiber to the probe end. Light reemitted by tissue is collected by the same probe and is guided via the other arm of the bifurcated fiber to the spectrograph, where spectral analysis is done of the collected light.

The amount of reflectance light measured, when applying the SFR technique, is influenced by three factors, which are:

- The transport of light in tissue.
- The dimensions of the fiber.
- The coupling of light into the fiber.

The transport of light in tissue depends on the scattering and absorption properties of light in tissue, as described in paragraph 2.1. These properties ultimately determine how much light is reemitted by tissue. Furthermore, only light that makes contact with the fiber face will have a chance to be coupled by the fiber. Finally, the coupling of light into the fiber is dependent on the

angular distribution of the light reemitted by tissue (which depends on the tissue scattering properties) and the fiber Numerical Aperture which will be defined in paragraph 3.1.

The amount of light that is absorbed in tissue is dependent on the path length that light propagates in tissue, as can be derived from equation 3. The path length is mainly determined by the scattering properties in tissue, which alter the propagation direction. This means that the light reemitted by tissue is mainly determined by the tissue scattering properties.

A semi-empirical model has been introduced by [2] to be able to describe the relation of scattering properties on the single fiber reflectance  $R_{SF}$  in absence of absorption. Before applying the model, the measured  $R_{SF}$  is first corrected for absorption as done in [3]. The model that describes the relation between the single fiber reflectance in absence of absorption,  $R_{SF}^{\circ}$ , and the scattering properties is defined by the following equations,

$$R_{SF}^{\circ} = \frac{TPC}{TPL} = \eta_c \Phi \quad (8)$$

$$\Phi = \frac{TPH}{TPL} \quad (9)$$

$$\eta_c = \frac{TPC}{TPH} = \eta_{lim}(1 + B) \quad (10)$$

Where:

$R_{SF}^{\circ}$	: The collected reflectance intensity without absorption	[-]
$\Phi$	: The fraction of photons reemitted, that hit the fiber face	[-]
$\eta_c$	: The collection efficiency	[-]
$TPC$	: The amount of photons collected by the fiber	[-]
$TPL$	: The amount of photons initially launched	[-]
$TPH$	: The amount of photons that hit the fiber face	[-]
$TPC$	: The amount of photons collected by the fiber	[-]
$B$	: An expression that is dependent on scattering properties	[-]
$\eta_{lim}$	: The collection efficiency limiting factor	[-]

As can be seen in equations 8 and 10  $\eta_c$  is the factor in that defines the maximum amount of light that is coupled by the fiber. A detailed description of  $\eta_c$  has previously been given by [4], in which has been observed that when measuring highly scattering media  $\eta_c$  approaches the limiting value  $\eta_{lim}$ , which is defined with the following expression,

$$\eta_{lim} \approx \sin(\alpha_{max}) \quad (11)$$

Where:

$\alpha_{max}$	: The maximum acceptance angle	[rad]
----------------	--------------------------------	-------

The maximum acceptance angle,  $\alpha_{max}$ , is dependent on  $NA$ . This dependency will be described in paragraph 3.1.

### 3. Light propagation in optical fibers

In this chapter the properties of an optical fiber are explained beginning with a brief explanation of light propagation in an optical fiber. Afterwards, the fiber Numerical Aperture is defined and the wavelength dependence thereof will be explained. Finally an explanation is given on cladding modes.

#### 3.1 Total Internal Reflection and fiber Numerical Aperture

An optical fiber consists of a cylindrical core of refractive index  $n_{co}$  with around it a cylindrical envelope of refractive index  $n_{cl}$  that is called the cladding. The refractive index of the cladding is smaller than the core refractive index ( $n_{cl} < n_{co}$ ).

Light can be propagated by the fiber core provided that it undergoes total internal reflection (TIR) at the core/ cladding interface. Furthermore, a distinction is made between two possible ways that light is able to be propagated, via TIR, in a fiber. These are described as meridional rays and skew rays. Meridional rays are rays that, when propagating, cross the fiber axis, whereas skew rays, when propagating, do not cross the fiber axis. These two types of rays are schematically illustrated in figure 2.

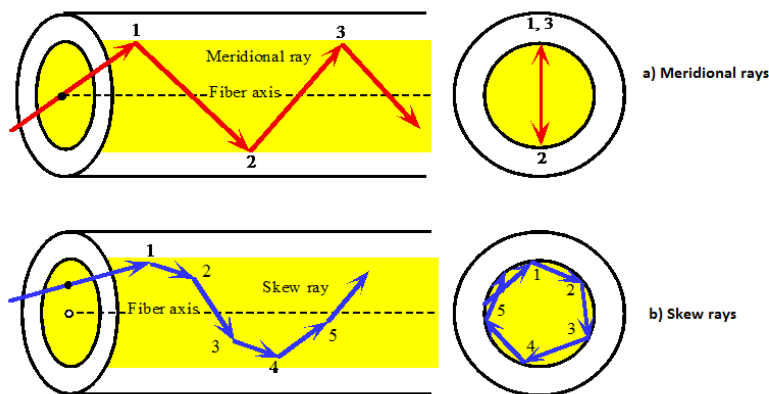


Figure 2: a). Meridional rays and b). Skew rays. From [5]

According to the law of refraction, TIR reflection occurs when the angle with which light is incident on the core/cladding interface obeys the following expression [6]:

$$\sin(\theta_i) \geq \frac{n_{cl}}{n_{co}} \quad (12)$$

in which,

$$\sin(\theta_c) = \frac{n_{cl}}{n_{co}} \quad (13)$$

Where:

$\theta_i$	: Incident angle of light on the core/cladding interface	[rad]
$\theta_c$	: The critical angle at which TIR occurs	[rad]
$n_{co}$	: The core refractive index	[-]
$n_{cl}$	: The cladding refractive index	[-]

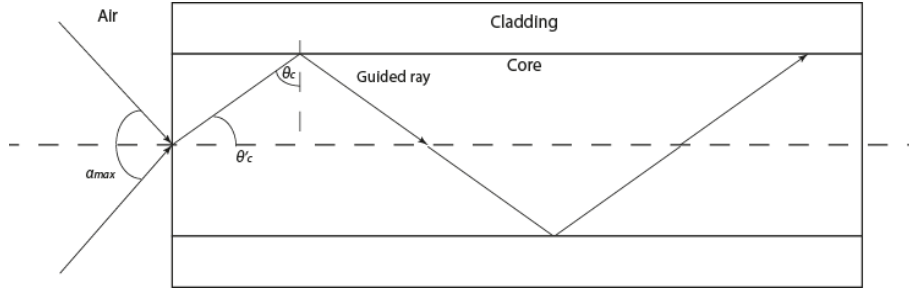


Figure 3: Ray model of light propagation in an optical fiber due to TIR.

The angle  $\theta_c$  can be written in terms of maximum angle of light incident on the core/air interface. This is done by defining the refraction of light, incident with the angle  $\alpha_{max}$  on the core/air interface, into the core with Snell's law,

$$n_0 \sin(\alpha_{max}) = n_{co} \sin(\theta'_c) \quad (14)$$

Where

$n_0$	: The outside medium refractive index (air in this case)	[1.00]
$\theta'_c$	: The angle made with the core axis	[rad]

From figure 3 it can be seen that,

$$\cos(\theta_c) = \sin(\theta'_c)$$

In which,

$$\cos(\theta_c) = \sqrt{1 - \sin(\theta_c)^2} \quad (15)$$

By filling equation 15 into the right part of equation 14, the following expression is obtained

$$n_0 \sin(\alpha_{max}) = n_{co} \sqrt{1 - \sin(\theta_c)^2} \quad (16)$$

By substituting equation 13 into equation 16 the following expression is obtained,

$$n_0 \sin(\alpha_{max}) = n_{co} \sqrt{1 - \left(\frac{n_{cl}}{n_{co}}\right)^2} = \sqrt{n_{co}^2 - n_{cl}^2} \quad (17)$$

Finally, the fiber Numerical Aperture is defined by the following expression,

$$NA = \sqrt{n_c^2 - n_{cl}^2} = n_0 \sin(\alpha_{max}) \quad (18)$$

Where:

$NA$ : The fiber Numerical Aperture

[—]

The  $NA$  is a characteristic property of the fiber that is defined by the refractive indices of core and cladding, as can be seen in equation 18.

It is known that all material media are dispersive, due to the dependence of refractive index on light frequency or, equivalently, wavelength [7]. This means that the  $NA$  will also be dependent on wavelength. The expected  $NA$  value and slope as function of wavelength for step index silica fibers have been reported in the literature. For example, dispersion measurements were done by J.W. Fleming and D.L. Wood on bulk samples of fluorine doped silica, which contained 1% and 2% fluorine [8]. The fluorine doped silica is normally used as cladding material, with pure silica as core material. This is done because of the slightly lower refractive index, in comparison with pure silica, that is obtained by doping silica with fluorine.

The bulk samples were fabricated in the form of prisms with apex angles of  $45^\circ$ . The refractive index dependence on wavelength was determined by measuring the deviation of monochromatic light that was shined on the prism specimen. This was done on prism specimens containing 1% and 2% doped silica for a series of wavelengths. Dispersion measurements were also done on samples of pure silica. The  $NA$  is then calculated, for each wavelength, from the measured refractive indices. The results plotted are shown in figure 4.

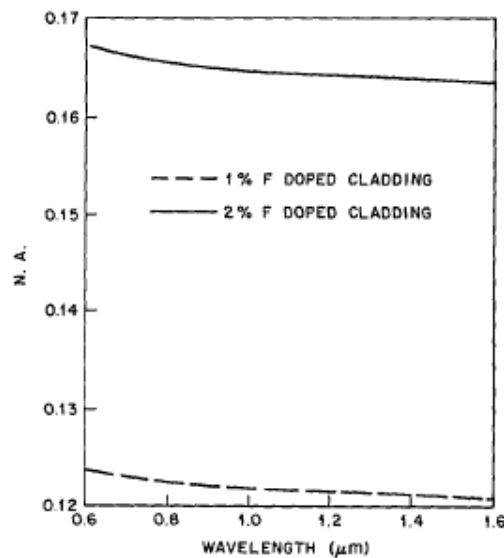


Figure 4:  $NA_{fib}$  dependence on wavelength for step index fibers with pure silica cores and 1% or 2% fluorine doped cladding. From [8]

Sladen et al. had similar  $NA$  measurement results [9]. Here  $NA$  was determined by measuring the optical throughput, that is dependent on  $NA^2$  [10]. The results reported are shown in figure 5.

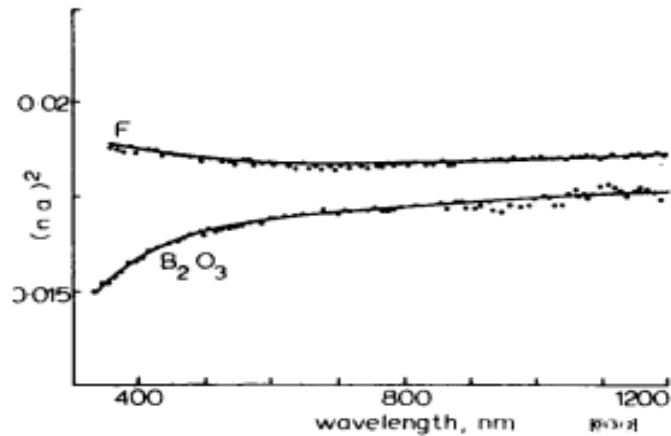


Figure 5: *NA* dependence on wavelength for two step-index fibers with pure silica cores and fluorine and boric oxide doped cladding. From [9]

Both results obtained from different papers and measured using different methods indicate that the *NA* of fused silica core, fluorine doped silica cladding have a decreasing *NA* slope with increasing wavelength in the visible wavelength range.

### 3.2 Cladding modes

When light is incident at an angle  $\alpha > \alpha_{max}$ , part of the light is internally reflected and guided in the core, and part of the light is refracted in the cladding and is propagated in the cladding as a cladding mode. This is illustrated in figure 6.

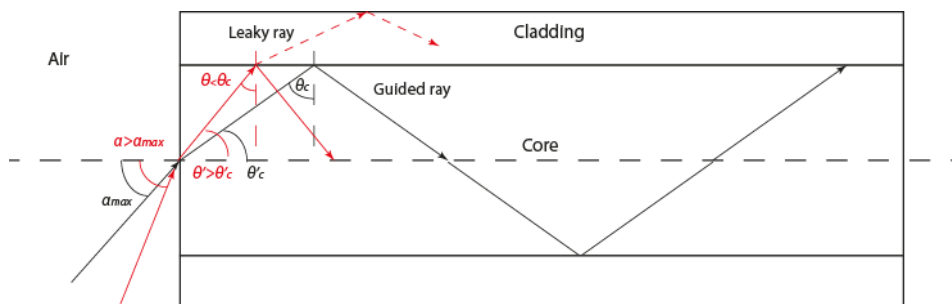


Figure 6: Ray model of light propagation in an optical fiber and cladding.

Light propagated by the cladding is usually not wanted and the fiber is coated with a polymeric layer that is called the buffer, which attenuates the light that is propagated by the cladding.

Studies have been done on the influence of cladding modes on the angular distribution of light exiting the fiber. An example is a study done, by R. Payne and L.O. Bouthillette to explain a secondary ring pattern observed in the fiber output radiation profile for sufficiently short optical fibers [11].

The study was done on two 2-m length, multimode, step-index fibers. One was stripped of cladding modes and the other was not. Furthermore,  $NA = 0.173$ , which corresponds to a maximum acceptance angle of  $\alpha_{max} = 9.96^\circ$ .

A collimated He-Ne laser source, at a wavelength of 632.8 nm, was used to illuminate the fibers. The laser incident illumination angle was varied from  $0^\circ$  to  $13^\circ$  and the fiber output profile was photographically recorded. The results are shown in figure 7.

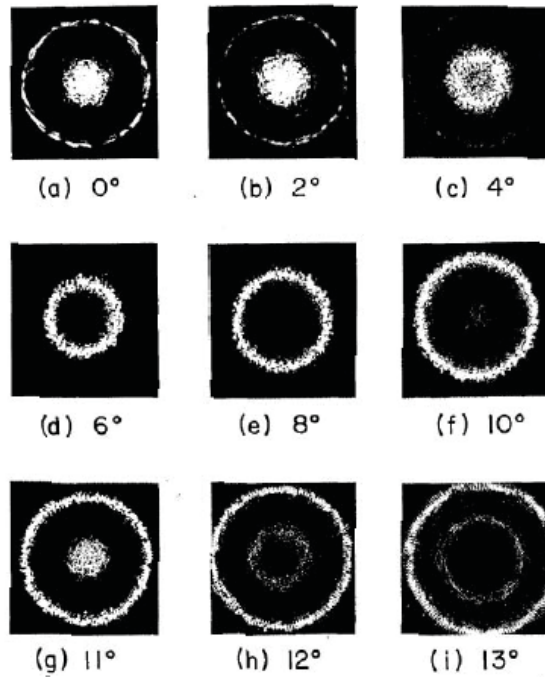


Figure 7: The photographically recorded far field patterns for laser incident angles of  $0^\circ$  to  $13^\circ$ . From [11]

The output profile is divided into a primary pattern and a secondary pattern. It has been observed that the output angle of light that forms the primary pattern corresponds to the incidence angle of light coupled into the fiber. On the other hand, output angles of light that forms the secondary pattern correspond to angles that are larger or smaller than the incidence angle of light coupled into the fiber. This is clearly seen in figure 7a, where light is coupled into the fiber at  $\alpha = 0^\circ$ . The center spot is the primary pattern and the faint ring at a larger angle is the secondary pattern. In addition, the output angle of light forming the secondary pattern in figure 7a has been measured to be approximately the same value as the maximum acceptance angle.

Furthermore, as the incidence angle increases, the angle of light forming the primary and secondary pattern also increases. This is true until the incidence angle approximates the maximum acceptance angle, which is illustrated in figure 7f. Here, light forming the secondary pattern is exiting the fiber at lower angles whereas light that forms the primary pattern is exiting the fiber at an angle equal to the incidence angle.

Additionally, it was observed that light forming the secondary pattern is absent when the fiber is very long or when a short fiber is stripped of cladding modes, which confirms that the secondary pattern is caused by cladding modes. This also indicates that cladding light is not properly attenuated by the buffer in sufficiently short fibers.

The formation of the primary and secondary patterns are described as follows,

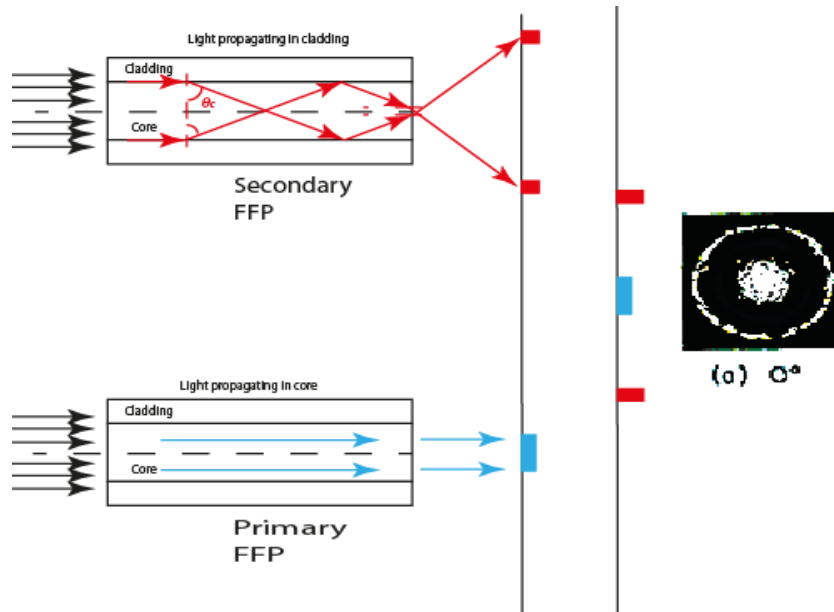


Figure 8: light incident at  $\alpha = 0^\circ$

Light forming the primary pattern is due to light that is propagated by the core and always corresponds to the angle of the incident light coupled into the fiber.

Furthermore, light forming the secondary pattern at angles smaller than the maximum acceptance angle is due to light that is incident in the cladding. This light is then refracted into the core at an angle equal to the critical angle, is propagated by the core and exits the fiber at an angle equal to maximum acceptance angle. This is illustrated in figure 8.

Moreover, as the incidence angle is increased light that enters the cladding will refract into the core at an angle larger than the critical angle and exit the core at an angle larger than the maximum acceptance angle.

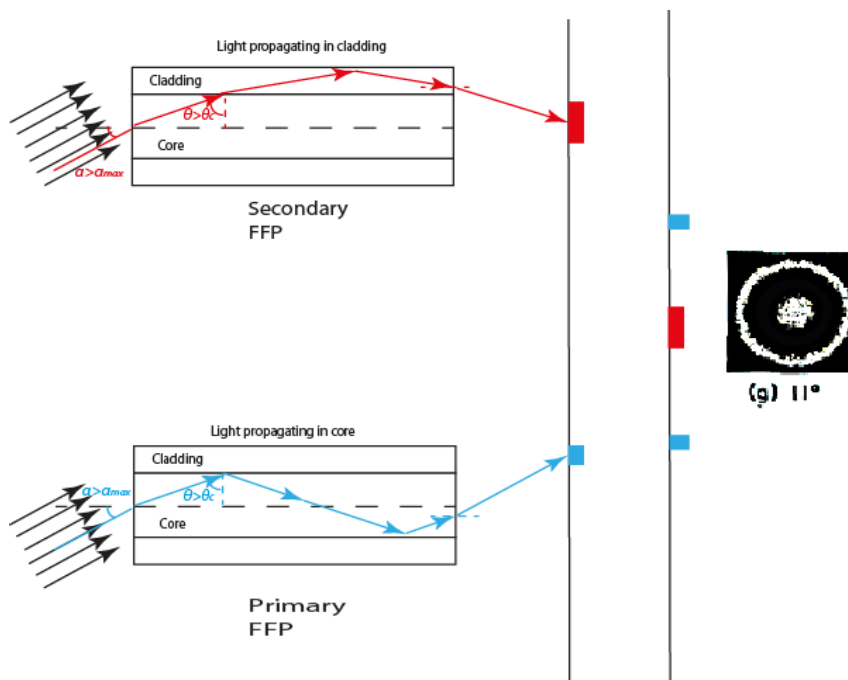


Figure 9: Light incident  $\alpha \geq \alpha_{max}$ .

Finally, when the incidence angle is equal to or larger than the maximum angle, light that refracts into the core will leak into the cladding since  $\theta < \theta_c$ . The fraction of this light that is propagated by the cladding will exit the cladding at lower angles, as illustrated in figure 9.

The angular distribution of light exiting the fiber is often measured to determine the  $NA$ , as will be described later on. Therefore, the expansion in this angular distribution caused by light propagating in the cladding can strongly influence the value measured for the  $NA$  and can lead to erroneous values for measured  $NA$ . Thus, measures have to be taken to remove the cladding modes.

## 4. Optical fibers and macro bending

Macro bending is referred to the act of bending an optical fiber with a constant bend radius. In this chapter, macro bending and the effects of macro bending, on the measured fiber output angle, are explained. Macro bending will be explained geometrically, in which a model is derived that describes the change in effective numerical aperture,  $NA_{eff}$ , as function of the radius of the bend induced on the fiber. Afterwards, an explanation is given on the wavelength dependence of  $NA_{eff}$  when a bend is induced on the fiber. This chapter is meant to give a basic understanding of effects that occur when inducing a bend on the optical fiber and will be used later on to qualitatively describe results obtained from the bending measurement.

### 4.2 Macro bending described geometrically.

Bending a fiber gives rise to loss of light due to the decoupling of light, which is propagated at angles near  $\theta'_c$ , from the core and radiated-off outside the core. Geometrically, this results in a change in maximum propagation angle in the core and leads to a change in,  $NA_{eff}$ .

A model has been developed by D.Gloge [12], that expresses bend losses in terms of a stronger attenuation of light that is propagated at angles near  $\theta'_c$ , as well as geometrically, by describing a reduction in maximum propagation angle caused by bending. The geometrical approach is adopted in which an expression is derived for the change in maximum propagation angle of light in the core in terms of induced bend radius. This expression is derived by means of ray optics as follows:

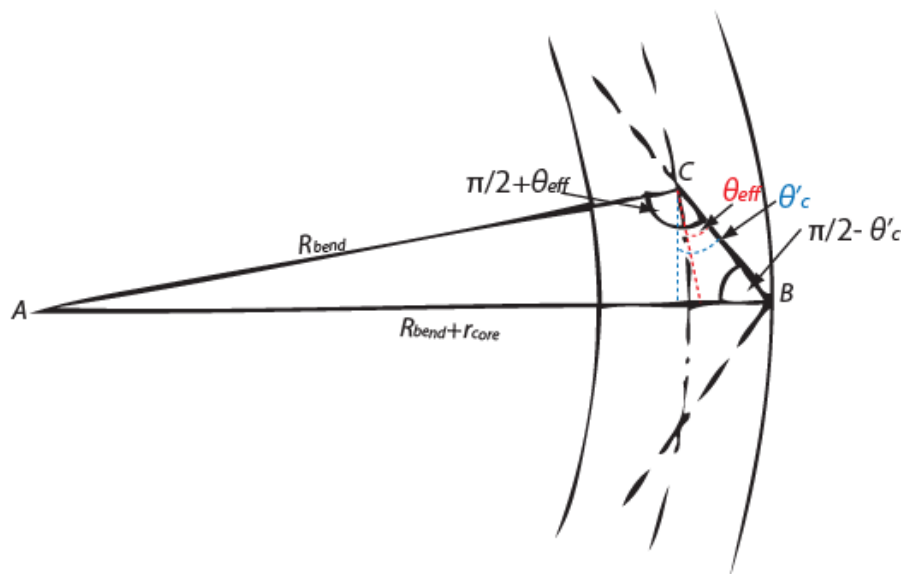


Figure 10: The change in propagation angle due to macro bending. From (12)

Consider a ray that is propagated by the core at an angle  $\theta'_c$ , with respect to the core axis. When the fiber is bent,  $\theta'_c$  is reduced to  $\theta_{eff}$ , which is the effective propagated angle due to bending. This is caused by the displacement of the core axis due to bending which is illustrated in figure 10.

By applying the sine rule to the triangle ABC, illustrated in figure 10, the following expression is attained,

$$\frac{\sin\left(\frac{\pi}{2} - \theta'_c\right)}{R_{bend}} = \frac{\sin\left(\frac{\pi}{2} + \theta_{eff}\right)}{R_{bend} + r_{core}} \quad (19)$$

Where:

$\theta_{eff}$	: The effective propagated angle	[rad]
$R_{bend}$	: The bend radius	[m]
$r_{core}$	: The core radius	[m]

The following trigonometric rule is then applied to equation 19,

$$\sin(x \pm y) = \sin(x) \cos(y) \pm \sin(y) \cos(x)$$

This gives the following equation:

$$\frac{\cos(\theta'_c)}{R_{bend}} = \frac{\cos(\theta_{eff})}{R_{bend} + r_{core}} \quad (20)$$

Equation 20 can be re-written to,

$$\cos(\theta_{eff}) = \left(\frac{R_{bend} + r_{core}}{R_{bend}}\right) \cdot \cos(\theta'_c) = \left(1 + \frac{r_{core}}{R_{bend}}\right) \cdot \cos(\theta'_c) \quad (21)$$

The small angle approximation is then applied to equation 21, which is given by the following equation,

$$\cos(\theta) = 1 - \frac{\theta^2}{2}$$

this gives the following,

$$1 - \frac{\theta_{eff}^2}{2} = \left(1 + \frac{r_{core}}{R_{bend}}\right) \left(1 - \frac{\theta_c'^2}{2}\right) \quad (22)$$

Equation 22 is reduced to,

$$\theta_{eff} = \theta'_c \sqrt{1 + \frac{r_{core}}{R_{bend}} - \frac{2r_{core}}{R\theta_c'^2}} \quad (23)$$

in which,

$$\frac{r_{core}}{R_{bend}} \approx 0$$

This results in the following,

$$\theta_{eff} = \theta'_c \sqrt{1 - \frac{2r_{core}}{R_{bend}\theta'^2_c}} \quad (24)$$

Because the angles that are going to be measured are relatively small, it can be assumed that:

$$\sin(\theta) \approx \theta$$

And by substituting,

$$\frac{NA_{eff}}{n_{co}} = \theta_{eff} \quad \& \quad \frac{NA}{n_{co}} = \theta'_c$$

In equation 24 because

$$NA = n_{co} \sin(\theta)$$

Equation 24 can be rewritten to:

$$NA_{eff} = NA \sqrt{1 - \frac{2r_{core}(n_{co})^2}{R_{bend}(NA)^2}} \quad (25)$$

Equation 25 describes the change in  $NA_{eff}$ , caused by inducing a bend with radius  $R_{bend}$  to the fiber. The derivation of equation 25 provides a basic understanding of which factors influence the change in  $NA_{eff}$ . This equation however is only applicable on large bends and will not be used to describe the changes in  $NA_{eff}$  from bending measurements performed in this study.

## 4.2 Wavelength dependent bending loss

When applying small bend radii to an optical fiber, oscillations that are wavelength dependent can be observed in the transmitted light. This wavelength dependent bend loss has been described in the literature. Morgan et al., for example, have accurately described the observed oscillatory patterns as interference between light that is refracted out of the core, due to the induced bend, and is propagated by the cladding or buffer and light that is propagated by the core [13]. In this description, light is envisioned as a plane wave type ray in which the electric field is parallel to the interface. Furthermore, in the theoretical model described, the cladding and the buffer have finite dimensions, as is so in practice. This model is shown In figure 11.

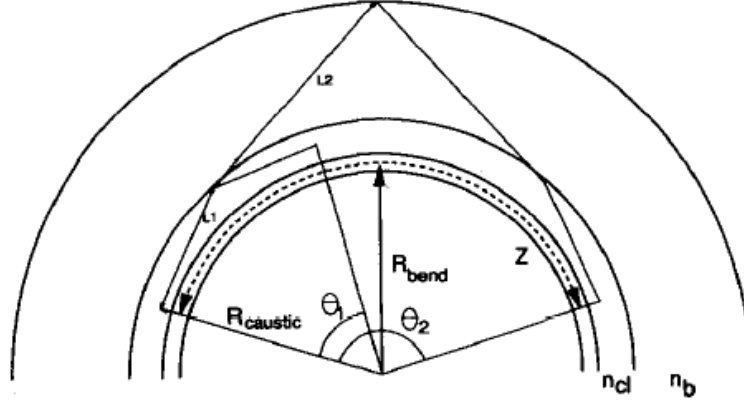


Figure 11: Schematic of fiber bend geometry and the formation of modes propagating in cladding and buffer. Only the outer layers have been drawn. From [13].

The following interference condition is introduced that gives a description of the wavelength dependent oscillations,

$$\frac{2\pi}{\lambda} l_j - \beta Z_j + \varphi_j = 2\pi m_j \quad (26)$$

Where:

$\lambda$	: The wavelength	[m]
$l_j$	: The optical path length of the $j_{th}$ mode group	[m]
$\beta$	: The propagation constant of modes guided by the core	[m <sup>-1</sup> ]
$Z_j$	: The optical path, over an angle $\theta_j$ length of the core modes	[m]
$\varphi_j$	: Phase constant due to TIR	[rad]
$m_j$	: An integer	[–]

In equation 26 and in figure 11, light propagated by the cladding is defined as mode group  $j = 1$  and light propagated by the buffer is defined as mode group  $j = 2$ .

Figure 11 shows, that mode group  $j = 1$  is caused by light that is reflected at the cladding/buffer interface and propagates a distance  $l_1 = 2L_1 n_{cl}$ , in which  $L_1$  is the distance travelled between core/cladding and cladding/buffer interface. Mode group  $j = 2$  is caused by light that is refracted from the cladding into the buffer, reflected at the buffer/air interface and propagates a distance  $l_2 = 2(L_1 n_{cl} + L_2 n_{bu})$ . Here  $L_2$  is the distance travelled between cladding/buffer and buffer/air interface and  $n_{bu}$  is the buffer refractive index.

The observed oscillations are caused by optical path length (OPD) differences between the cladding/buffer and the core guided modes. When varying the wavelength, changes in the relative phase are introduced, which lead to oscillations in the bend loss.

The results obtained by Morgan et al. are illustrated in figure 12.

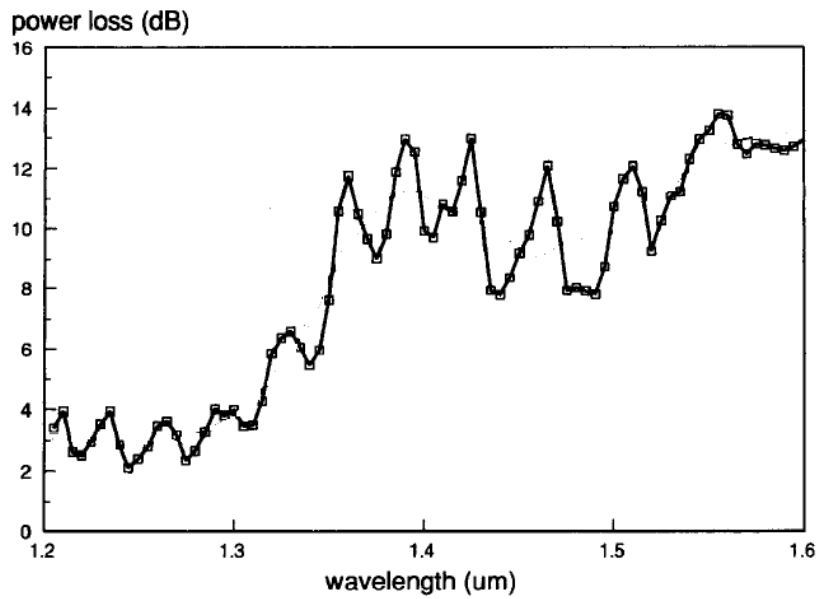


Figure 12: Bend loss dependence on wavelength in a buffered fiber, for 180° bend of 5.5 mm radius. From [13]

The oscillatory, wavelength dependent, bend loss, illustrated in figure 12 can be divided into two distinct components, a slow oscillating pattern and a fast oscillating pattern. It has been shown that the slow oscillating pattern is caused by light that is reflected at the cladding/buffer interface and interferes with light propagated by the core, and the fast oscillating pattern is caused by light that is reflected at the buffer/air interface and interferes with light propagated by the core.

## 5. Materials and methods

This chapter describes the measurement setups and methods used to measure  $NA$  and its dependence on wavelength and bend radius. A description is also given of the components used to build up the different measurement setups.

### 5.1 Fiber Numerical Aperture measurements

#### 5.1.1 Measurement method

The  $NA$  is measured by making a scan of the fiber output profile in the far field region. This is illustrated in figure 13.

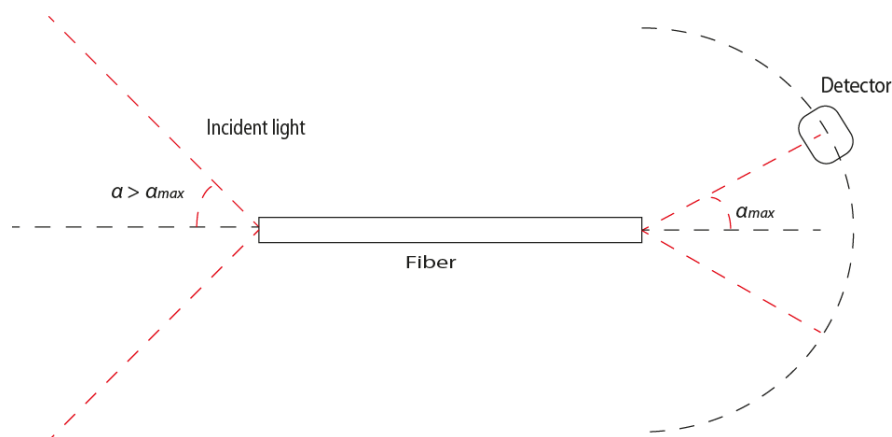


Figure 13: A schematic of the far field scan technique

As can be seen in figure 13, the fiber is illuminated at the proximal end by an overfilled launch condition, which means that light illuminating the fiber will be incident at angles  $\alpha > \alpha_{max}$ . By doing this, light will exit the fiber with an angle  $\alpha_{max}$ . The illumination spot of light incident on the fiber is made smaller than the core diameter to avoid the launch of light in the cladding, which can disturb the  $NA$  measurements.

Furthermore, a detector is placed at a distance that is defined to be the far field region. Literature states that the far field region of an electromagnetic source is calculated with the following equation [14]:

$$z_{FF} > \frac{d_{fib}^2}{\lambda} \quad (27)$$

Where:

$z_{FF}$	: The theoretically defined Far Field distance	[m]
$d_{fib}$	: The fiber core diameter	[m]

The distance of the far field region for each of the measurement fibers is calculated in appendix II.1. The detector is used to scan the fiber output intensity profile and  $NA$  is defined as the sine of the angle where the intensity has dropped to 5% of the maximum intensity value. This is an empirical value that has been determined from a large amount of measurements done with silica fibers.

### 5.1.2 Measurement setup

The measurement setup used for the  $NA$  measurement is shown in figure 14.

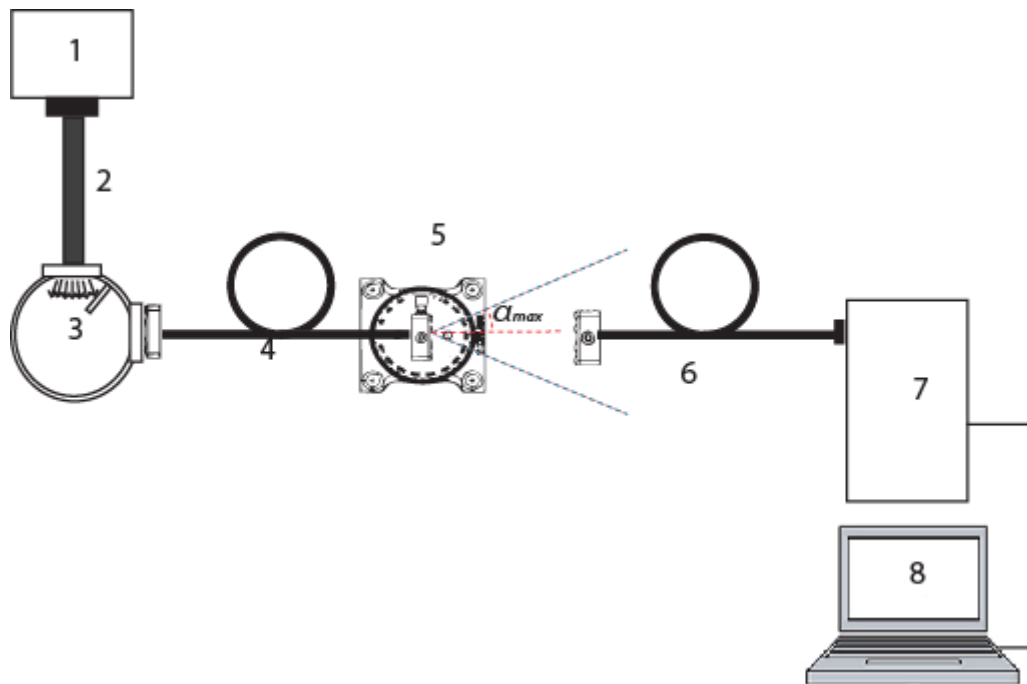


Figure 14: A schematic of the Far Field scan measurement setup.

Table 1 lists the components used to build up the measurement setup schematically illustrated in figure 14 .

Table 1: List of components used to build up the far-field measurement setup.

#	Components	Specifications	
1	<b>Lamp</b>	Brand	Thorlabs
		Type	Halogen
		$P_{output}$	150 W
2	<b>Integrating sphere</b>	Brand	Oriel
		Radius	$7.6 \cdot 10^{-2}$ m
3	<b>pinhole setup</b>	—	—
4	<b>Measurement fibers</b>	Brand	Ocean optics
		$d_{fib}$	200 $\mu$ m & 400 $\mu$ m
		Specified $NA$	$0.22 \pm 0.02$
		Brand	Avantes
		Fiber core diameters	800 $\mu$ m
		Specified $NA$	$0.22 \pm 0.02$
5	<b>Rotational stage.</b>	Radial scale spacing	$2^\circ$
6	<b>Detection fiber</b>	Brand	Ocean optics
		$d_{fib}$	400 $\mu$ m
7	<b>Spectrograph.</b>	Brand	Ocean Optics
		Type	QE65000
		Spectral Range	200-1100 nm
		Resolution	0.796 nm
8	<b>Computer</b>	Acquisition software	Labview Version 7.1
		Analysis software	Matlab Version R2010a, Math Works

In this measurement setup light from the halogen lamp is coupled into the integrating sphere where the angular intensity distribution of the halogen lamp is converted into diffuse light. This is done in order to ensure that the  $NA$  measurements are not disturbed by the characteristic halogen lamp spatial intensity distribution.

Moreover, a pinhole is placed in front of the input end of the measurement fiber to prevent light from being launched into the cladding, which ensures that the measurements are not influenced by cladding modes. To be able to align the pinhole with the measurement fiber input end, the pinhole and fiber are incorporated into a pinhole setup. The pinhole setup design is explained in detail in appendix III.

The output end of the fiber is mounted into an x-y translational optical mount which is mounted onto the rotational stage. The fiber radiation profile is scanned onto the detection fiber by rotating the stage. The light coupled into the detection fiber is then transported to the spectrograph which measures the intensity value of the different wavelength components of the coupled light. The measured intensity levels and corresponding wavelengths are acquired with Labview and data analysis is done with Matlab.

### 5.1.3 Measurement Procedure

Fiber diameters of  $d_{fib} \in [200\ 400\ 800]$   $\mu\text{m}$  are investigated in this study. Pinhole diameters of  $d_{pinhole} \in [100\ 150]$   $\mu\text{m}$  are used to prevent light from being coupled by the cladding. The spectral dependence of the  $NA$  will be measured in the spectral range of  $\lambda \in [400 - 900]$  nm.

To investigate the effect of cladding modes on the angular distribution of light exiting the measurement fiber, measurements are done with and without a pinhole placed at the fiber proximal end.

When measuring with a pinhole at the fiber proximal end, the fiber radiation profile is scanned over a range of  $16^\circ$  on both sides of the radiation pattern. This corresponds to an output numerical aperture,  $NA_{out} \approx 0.28$ . When measuring without a pinhole at the fiber proximal end, the fiber radiation profile is scanned over a range of  $26^\circ$  on both sides of the radiation pattern. This corresponds to an output numerical aperture,  $NA_{out} \approx 0.44$ .

The rotational stage is scaled in steps of  $2^\circ$ , but to be able to measure  $\alpha_{max}$  as accurately as possible, measurements are made every  $1^\circ$  in the region where the profile has dropped below 10% of the maximum profile intensity. The maximum readout error is half of the step between scales, which is  $1^\circ$ .

Errors due to lamp fluctuation, shot noise and thermal noise are accounted for by taking the following steps: The detector in the spectrograph is cooled to a temperature of  $-20^\circ\text{C}$  in order to reduce thermal noise to a minimum. Furthermore, three measurements are taken at each angle and are averaged in order to average out inaccuracies due to lamp fluctuations, shot noise and thermal noise. Finally, three measurements are taken of the dark noise and are averaged and subtracted from the profile measurements.

Alignment errors are accounted for by taking the following steps: The acceptance angle of both sides of the profile are determined, summed and averaged to correct for horizontal profile alignment error. Other alignment errors, which are the vertical alignment error of the detection fiber with the center of the radiation profile and the error in alignment of the fiber with the rotational stage axis, are calculated with expressions derived in appendix II.3 and Appendix II.2, respectively.

The results are illustrated in paragraph 6.1 and explained in paragraph 7.1.1.

## 5.2 CCD camera measurements

### 5.2.1 Measurement method

The fiber radiation pattern was also measured with a CCD camera in order to validate the spectrally measured  $NA$  and to show what influences cladding modes have on the measured profile, when no pinhole is placed at the fiber proximal end. The fiber radiation pattern is imaged on a CCD camera. A line profile is then applied on the images, wherein the maximum intensity is determined and the radius where the intensity has dropped to 5% is calculated. The maximum acceptance angle is then calculated with the following equation:

$$\tan^{-1}\left(\frac{r_{profile}}{z}\right) = \alpha_{max} \quad (28)$$

Where:

$z$  : The distance between fiber and detector [m]  
 $r_{profile}$  : The profile radius [m]

The  $NA$  is then calculated with equation 18.

### 5.2.2 Measurement setup

Slight modifications were made to the measurement setup described in paragraph 5.1. The measurement setup used is shown in figure 15.

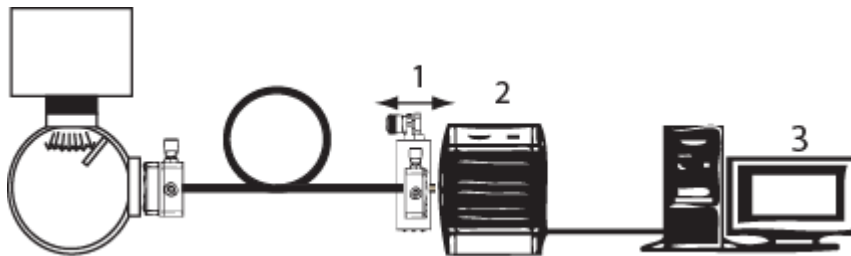


Figure 15 : A schematic of the CCD measurement setup.

The components used to make the CCD camera setup are listed in table 2.

Table 2: List of components used to build up the CCD camera setup.

#	Components	Specifications	
1	<b>Translational stage</b>	Brand	Uniphase
2	<b>CCD camera</b>	Brand	Hamamtsu
		Type	ORCA-ER
3	<b>Computer</b>	Acquisition software	Wasabi Version 1.5
		Analysis software	Image J Version 1.45s

The detection fiber and spectrograph are replaced by a CCD camera and the rotational stage is replaced by a translational stage. Due to the small dimensions of the CCD element, the fiber is

placed close to the CCD camera in order to be able to fully image the radiation profile. The camera is remotely controlled by desktop computer running the camera software, Wasabi.

Snapshots are taken of the radiation profile emitted by the fiber. These are saved in TIFF format, to ensure no loss of image information. Image analysis is done in image J, which is an image processing and analysis program.

### 5.2.3 Measurement procedure

The camera is a hermetically sealed system and a planar glass slab is placed at an unknown distance in front of the CCD element which enables light to pass through. Because the distance from the glass slab to the CCD element is not known, a translational stage is used to vary the distance between fiber and CCD element. A change in measurement fiber/CCD element separation will correspond to a linear change in profile radius.

Before measuring a series of 20 snapshots are taken and averaged when the light source is turned off. The averaged image is applied as background subtraction.

During measurement, the distance between measurement fiber and CCD element is varied in the range of  $z \in [0.00 - 3.50] \cdot 10^{-3}$ . This is done in steps of  $0.5 \cdot 10^{-3}$  m. At each position a series of 20 snapshots are taken of the measurement profile and are averaged. This is done in order to average out shot noise and thermal noise. Additionally, the detector is cooled to a temperature of  $-20$  °C, which keeps thermal noise at a minimum.

In order to determine the profile radius, line profiles are made of the CCD images in image J. Before applying a line profile, each image is scaled to the metrical CCD element dimensions. This enables the extraction of the profile radius in meters.

The profile radius will be determined for both sides of the profile and the values for the radii are summed and averaged to account for minor angular misalignments between the CCD camera and measurement fiber.

The value of  $\alpha_{max}$  is then calculated with equation 28 as follows:

$$\tan^{-1}\left(\frac{r_{21}}{z_{21}}\right) = \alpha_{max}$$

Where:

$r_{21}$ : Difference in profile radius between two measurement points [m]

$z_{21}$ : Difference in measurement distance between two measurement points [m]

The  $NA$  is calculated afterwards with equation 18.

An expression for the error in the calculated angle and  $NA_{fib}$  is derived and the errors are calculated in appendix II.4.

In addition, the CCD camera is not able to measure the spectral dependence of the  $NA$  which means that the value of the  $NA$  acquired with the CCD measurement setup is the average  $NA$ .

The results are presented in paragraph 6.2 and explained in paragraph 7.1.2.

## 5.3 Macro bending measurements

### 5.3.1 Measurement method

Fiber bending can be measured by wrapping the fiber around mandrels with of radii or with a two point bending system where a loop of the fiber is constrained between two faceplates and the faceplates are brought together.

When using mandrels to induce a bend in a fiber, the fiber is wrapped around the mandrel with a known radius. Mandrels are substituted with one another to measure at different bend radii. Tension is applied to ensure that the fiber follows the mandrel profile. On the other hand, when using the two point bending system a fiber is placed in grooves that are engraved in the faceplates. These faceplates are then closed to obtain different bend radii.

In this study a two point bending system is used to induce bends on the fiber. This choice is made because measuring with the two point bending is less labor intensive and less time consuming.

Furthermore, it is possible to apply arbitrary bend radii to the fiber, this in contrast to being limited to a small amount of radii when using mandrels.

### 5.3.2 Measurement setup

A two point bend system is incorporated into the far field scan setup, illustrated in Figure 14. The setup used to measure fiber  $NA_{eff}$  dependence on bend radius is shown figure 16,

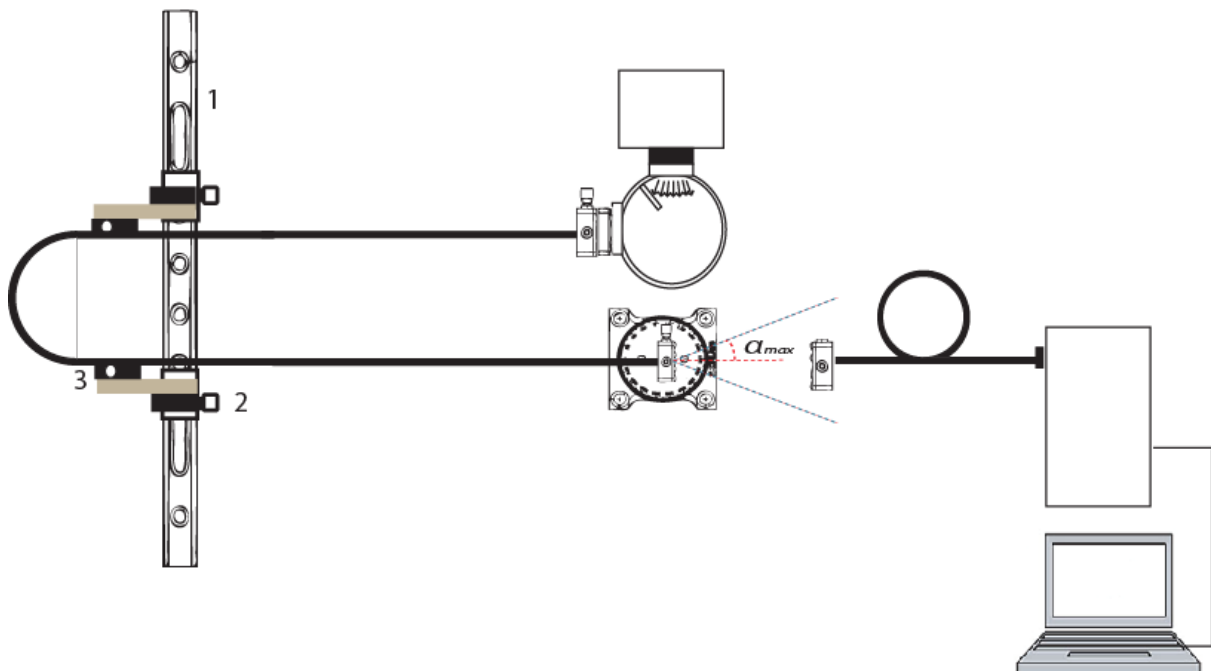


Figure 16: Macro bending measurement setup.

The components incorporated the far field scan setup are listed in table 3.

Table 3: List of components used to build up the Macro bending measurement setup.

#	Components	Specifications	
1	<b>Optic rail</b>	Brand	Parker, Daedal Division
2	<b>Optic railcomponent</b>	Brand	Parker, Daedal Division
3	<b>Filter holder</b>	Brand	Spindler and Hoyer

The two point bend system consists of a micro optical rail, two optical rail components on which post holders have been attached, two mounting posts, two optic mounts, two rectangular metal plates and two fixed filter mounts, that are applied as grooves.

The filter mounts are screwed on to the rectangular plates and the plates are then fastened on to the optic mounts. The mounting posts are then screwed on to the optic mounts and are then placed into the post holders that are attached to the optic rail components.

A loop is made in the fiber, and each side of the loop is then placed into a filter holder. The filter holders have clamps which are used to constrain both sides of the fiber. One of the optical rail components is then constrained to a fixed position while the bend radius is changed by moving the other optic rail component.

A profile scan, as explained in Paragraph 5.1.1, is performed to extract the wavelength dependent  $NA_{eff}$  at each bend radius. Data acquisition is done with Labview and data analysis is done in Matlab.

### 5.3.3 Measurement procedure

Bending measurements are done on  $d_{fib} \in [200 \ 400 \ 800] \mu\text{m}$ , in which a  $150 \mu\text{m}$  pinhole is placed in front of the 400 and  $800 \mu\text{m}$  fibers and a  $100 \mu\text{m}$  pinhole in front of the  $200 \mu\text{m}$  fiber.

A series of 5 measurements are performed per fiber, each with a bend of arbitrary radius induced on the fiber. The spectrally dependent  $NA_{eff}$  is then extracted according to procedure explained in paragraph 5.1.3.

The values for the  $NA_{eff}$  extracted at different bend radii are compared per fiber, to investigate the dependence of  $NA_{eff}$  on wavelength and bend radius. The error in extracted  $NA_{eff}$  will be determined in the same way as explained in paragraph 5.1.3. But since a series of bend measurements will be plotted in the same figure for comparison, the error bars will be omitted for figure clarity. The results are presented in paragraph 6.3 and explained in paragraph 7.1.3.

## 6. Results

In this chapter measurement results are presented for the  $NA$  measurements, the CCD measurements and the fiber bending measurements.

### 6.1 Fiber $NA$ measurements.

The  $NA$  measurements were done according to the procedural description in paragraph 5.1.3

Results for the 200 & 400  $\mu\text{m}$  fibers at various measurement and detection fiber distances are shown in figure 17.

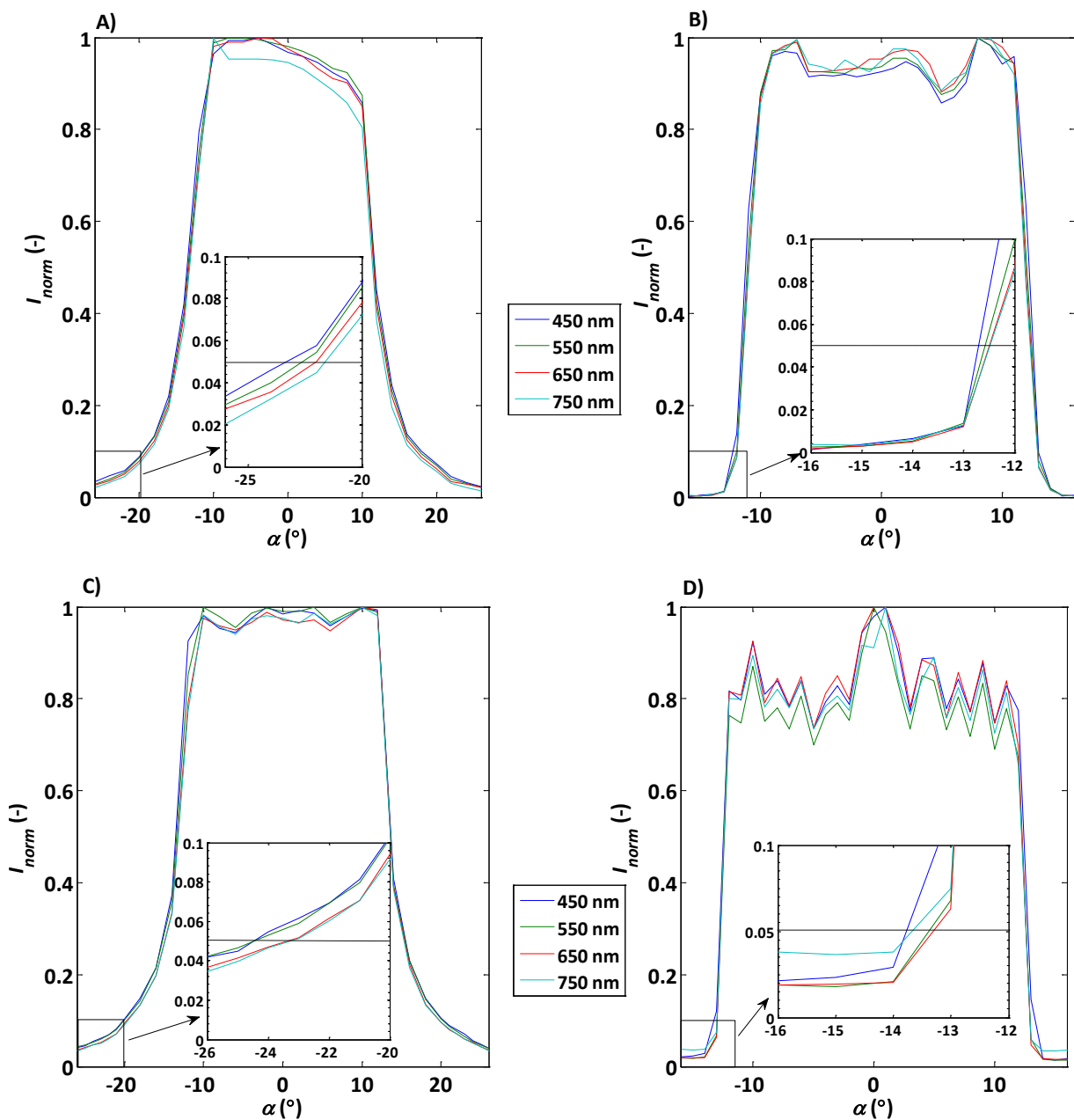


Figure 17: Normalized measured profile for a 200  $\mu\text{m}$  fiber with (B) & without (A) a 100  $\mu\text{m}$  pinhole at the proximal end and normalized measured profile for a 400  $\mu\text{m}$  fiber with (C) & without (D) a 150  $\mu\text{m}$  pinhole at the proximal end.

Figure 17.A and B illustrate profiles measured, at  $\lambda \in [450 \text{ } 550 \text{ } 650 \text{ } 750] \text{ nm}$ , for a  $200 \text{ }\mu\text{m}$  fiber with and without pinhole and figure 17C and D illustrate profiles measured at the same wavelengths for a  $400 \text{ }\mu\text{m}$  fiber with and without pinhole.

It can also be seen that the profiles measured for both fibers without pinhole are wider than the profiles measured with a pinhole. Also, the edges of the profiles measured with the pinholes are much steeper than the profile measured without pinholes. Cladding modes are the cause of the differences seen between the profiles measured with and without pinholes. This will be seen more clearly in the CCD images illustrated in paragraph 6.2.

A difference in profile peaks can be seen in figure 17 between measurements performed on fibers with and without pinhole. The change in profile shape is caused by diffraction at pinhole surfaces. This will be explained in paragraph 7.1.1. Measurements were done to investigate the effect that diffraction at the pinhole surface has on the  $NA$  extracted. Results are shown in figure 19.

Low signal was a problem when measuring at large fiber/ detector separations. Integration times used to increase the detected signal varied from  $2000 \text{ ms}$  to  $10000 \text{ ms}$ , which showed a minimal change in detected signal. This is why it was chosen to do measurements with smaller fiber/ detector separations. Measurements with the  $200 \text{ }\mu\text{m}$  fiber were done at a measurement-detection fiber distance  $z = 7.0 \cdot 10^{-2} \text{ m}$  and measurements done with the  $400 \text{ }\mu\text{m}$  fiber were done a measurement-detection fiber distance  $z = 26.6 \cdot 10^{-2} \text{ m}$ . The separations between the measurement and detection fiber in the measurements done with both the fibers are both smaller than the theoretically calculated far field distances listed in table 8. Therefore, measurements were done to investigate the change in  $NA$  when measuring with fiber/ detector separations smaller than the far field distances listed in table 8. Results are shown in figure 20.

The  $NA$  extracted from the radiation profiles shown figure 17 are presented in figure 18.

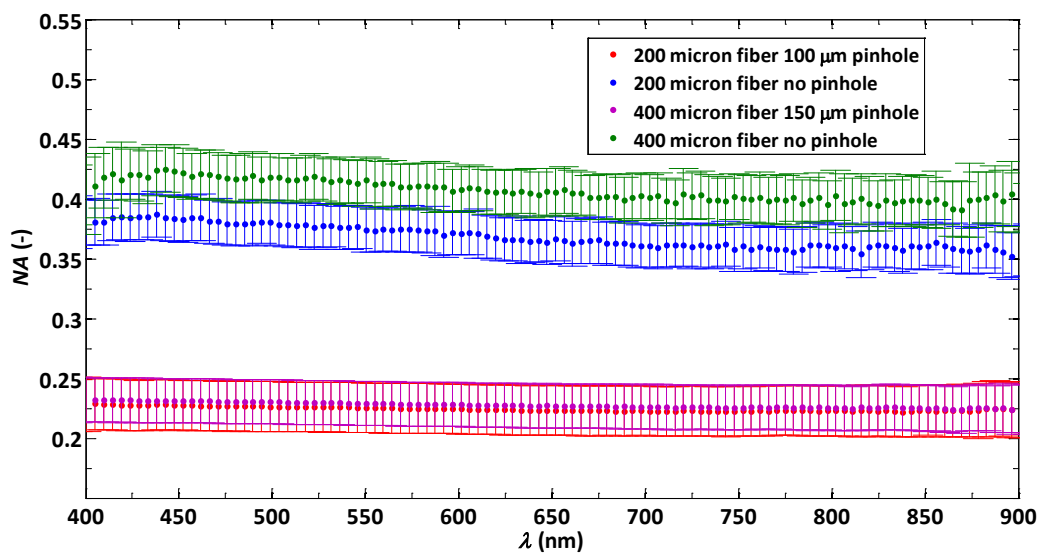


Figure 18: Numerical Apertures measured in the spectral range of  $\lambda \in [400 - 900] \text{ nm}$  for a  $200$  and  $400 \text{ }\mu\text{m}$  fiber with and without pinhole.

Each data point shown in figure 18 is an average of 6 other data points and the standard deviations of the averages taken are incorporated along with readout errors into the measurement error bars. This has been done for all results shown in this paragraph. The systematic error caused by measurement fiber/rotational stage axis misalignment, is listed in table 4.

Table 4: The calculated offset due to misalignment with the rotational stage axis for the results illustrated in figure 18

Measurement:	$z(10^{-2} \text{ m})$ $\pm 10^{-3} \text{ m}$	$NA_{average}$ (-)	$\alpha_{axerr}$ ( $10^{-3} \text{ rad}$ )	$NA_{axerr}$ ( $10^{-3}$ )
200 $\mu\text{m}$ fiber, 100 $\mu\text{m}$ pinhole	7.00	0.221	$\pm 3.2$	$\pm 3.2$
400 $\mu\text{m}$ fiber, 150 $\mu\text{m}$ pinhole	26.6	0.222	$\pm 0.9$	$\pm 0.9$

The systematical error caused by vertical misalignment of the radiation profile with the detection fiber is assumed to be 10% of  $NA_{average}$  at the most, which leads to  $NA_{verterr} \approx -0.023$ .

Figure 18 shows that, when no pinhole is used, light will exit the fiber at larger angles. Furthermore it can be seen that there is stratification in  $NA$  between the 200 and the 400 micron fiber, which will be explained in paragraph 7.1.1. On the other hand, it can be seen that  $NA$  values measured for both fibers, with pinhole, are in agreement with the  $NA$  value specified by the manufacturer.

The measurements to investigate the change in  $NA$  caused by diffraction at the pinhole surface were performed with different fiber diameters and pinhole sizes. The results are shown in figure 19.

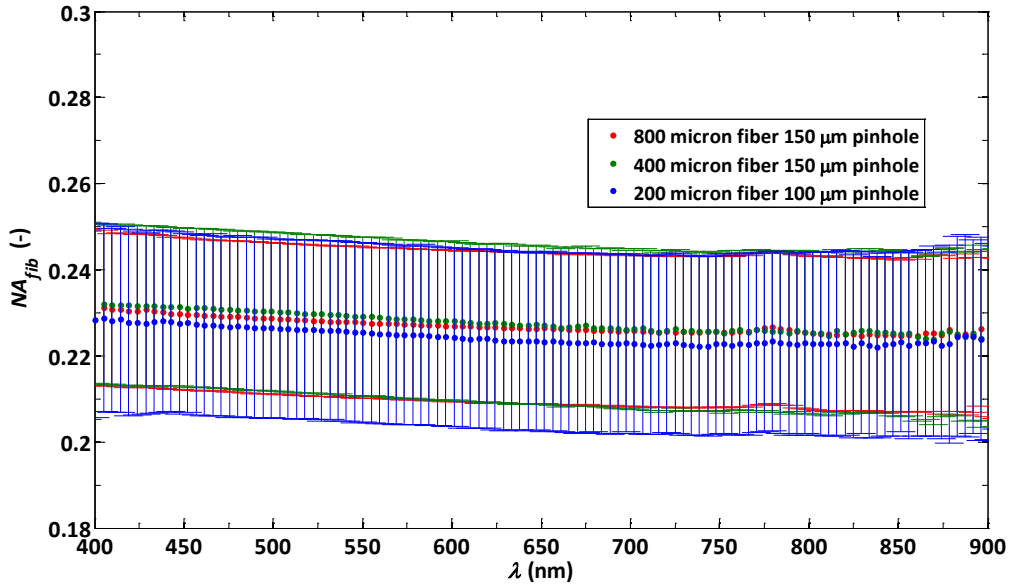


Figure 19: Numerical Apertures measured in the spectral range of  $\lambda \in [400-800] \text{ nm}$  for a 200, 400 and 800  $\mu\text{m}$  fiber with 100 and 150  $\mu\text{m}$  pinholes.

The pinholes were aligned with the help of the spectrograph. This is done by positioning the rotational stage at angle which is slightly larger than the expected  $\alpha_{max}$ . The fiber position is then adjusted until a minimum intensity value is measured with the spectrograph.

The investigation was limited to  $d_{pinhole} \leq 150 \mu\text{m}$  due to measurement disturbances caused by light exiting the fiber at higher angles when measuring with  $d_{pinhole} > 150 \mu\text{m}$ . This will be explained in Paragraph 7.1.1.

The results in figure 19 show that diffraction effects on the measured  $NA$  are negligible. Also, it can be seen that all results are in agreement with the manufacturer defined  $NA$ .

Errors caused by axial misalignment are listed in table 5.

Table 5: The calculated offset due to misalignment with the rotational stage axis for the results illustrated in figure 19

Measurement:	$z(10^{-2} \text{ m})$ $\pm 10^{-3} \text{ m}$	$NA_{average}$ (-)	$\alpha_{axerr}$ ( $10^{-3} \text{ rad}$ )	$NA_{axerr}$ ( $10^{-3}$ )
200 $\mu\text{m}$ fiber, 100 $\mu\text{m}$ pinhole	7.00	0.221	$\pm 3.2$	$\pm 3.2$
400 $\mu\text{m}$ fiber, 150 $\mu\text{m}$ pinhole	26.6	0.222	$\pm 0.9$	$\pm 0.9$
800 $\mu\text{m}$ fiber, 150 $\mu\text{m}$ pinhole	17.5	0.226	$\pm 1.3$	$\pm 1.3$

The measurements done to investigate the change in extracted  $NA$  were performed for different measurement/ detection fiber separations. The results are shown in figure 20.

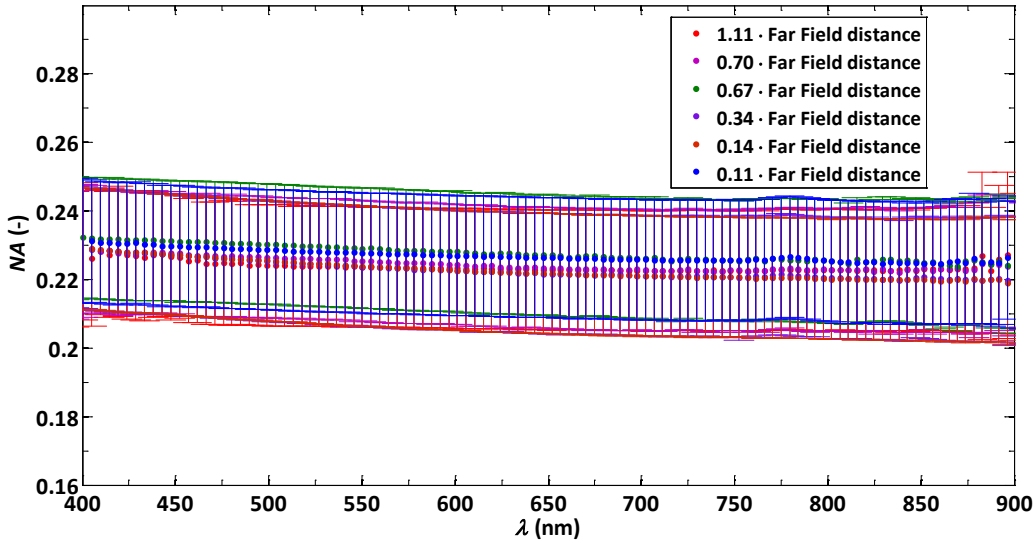


Figure 20: Numerical Apertures measured in the spectral range of  $\lambda \in [400-800] \text{ nm}$  for a 200, 400 and 800  $\mu\text{m}$  fiber at a range of  $\frac{z}{z_{FF}}$ .

Since the results shown in figure 20 are from measurements done with different fiber diameters it was chosen to display the results in ratio of  $z/z_{FF}$ . The fiber diameters, pinhole and distances corresponding to the different  $z/z_{FF}$  are listed in table 6.

Table 6: The calculated offset due to misalignment with the rotational stage axis for the results illustrated in figure 20

Measurement:	$z(10^{-2} \text{ m})$ $\pm 10^{-3} \text{ m}$	$\frac{z}{z_{FF}}$ (-)	$NA_{average}$ (-)	$\alpha_{axerr}$ ( $10^{-3} \text{ rad}$ )	$NA_{axerr}$ ( $10^{-3}$ )
200 $\mu\text{m}$ fiber, 100 $\mu\text{m}$ pinhole	11.1	1.11	0.219	$\pm 2.0$	$\pm 2.0$
200 $\mu\text{m}$ fiber, 100 $\mu\text{m}$ pinhole	7.0	0.70	0.221	$\pm 3.2$	$\pm 3.2$
400 $\mu\text{m}$ fiber, 150 $\mu\text{m}$ pinhole	26.6	0.67	0.222	$\pm 0.9$	$\pm 0.9$
400 $\mu\text{m}$ fiber, 150 $\mu\text{m}$ pinhole	13.5	0.34	0.221	$\pm 1.6$	$\pm 1.6$
400 $\mu\text{m}$ fiber, 150 $\mu\text{m}$ pinhole	5.7	0.14	0.222	$\pm 3.9$	$\pm 3.9$
800 $\mu\text{m}$ fiber, 150 $\mu\text{m}$ pinhole	17.5	0.11	0.226	$\pm 1.3$	$\pm 1.3$

The results in figure 20 show that the measured  $NA$  is not affected by measuring at distances  $z < z_{FF}$ . All results are in agreement with the manufacturer specified  $NA$ .

## 6.2 CCD camera measurements.

The CCD measurements are performed on a 200  $\mu\text{m}$  fiber with and without a 100  $\mu\text{m}$  pinhole at the fiber proximal end. The measurement is done in accordance to the procedural description in paragraph 5.2.3. Results for the determined radii at different fiber/detector separations are listed in table 7.

Table 7: The determined profile radii at different measurement fiber/ detector separations

#	$z(10^{-3} \text{ m})$ $\pm 10^{-5} \text{ m}$	$r_{left}(10^{-3} \text{ m})$ $\pm 10^{-5} \text{ m}$	$r_{right}(10^{-3} \text{ m})$ $\pm 10^{-5} \text{ m}$	$r_{average}(10^{-3} \text{ m})$ $\pm 10^{-5} \text{ m}$
1	0	3.9	3.9	3.9
2	0.5	4.03	4.03	4.03
3	1	4.14	4.17	4.16
4	1.5	4.24	4.32	4.28
5	2	4.38	4.42	4.4
6	2.5	4.47	4.56	4.515
7	3	4.59	4.68	4.635
8	3.5	4.66	4.85	4.76

Since the fiber was placed close to the CCD detector, a plot is made of the change in average profile radius due to a change in fiber/detector separation. This is done to show that the measurements do not suffer from any nonlinear diffractive effects. This is shown in figure 21.

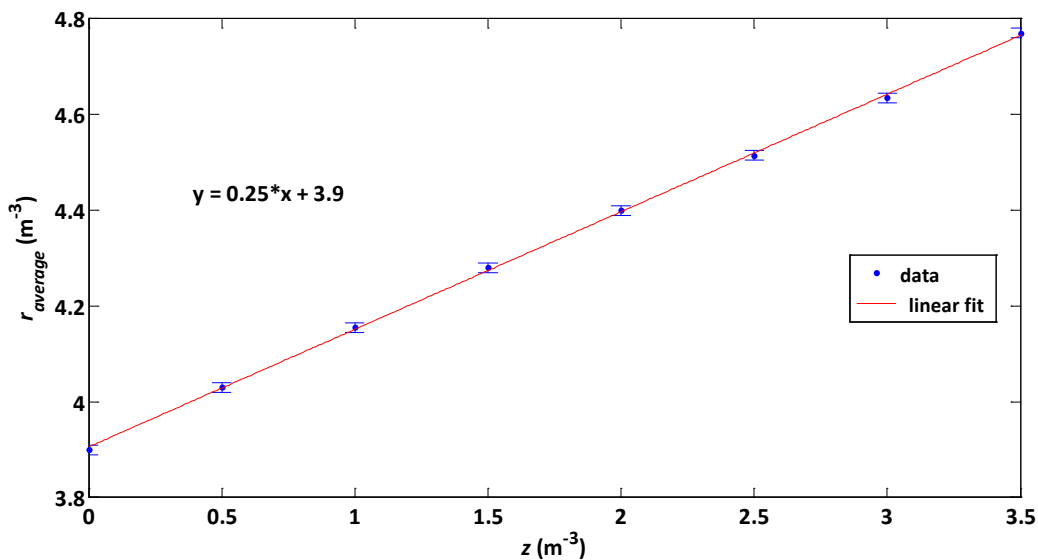


Figure 21 : The average profile radius as function of measurement fiber/ detector separation

It can be seen in figure 21 that the change in profile radius caused a change in fiber/ detector separation is a linear relationship, which is expected. The linearity is validated by applying a linear fit through the data points. This leads to the fit function displayed in figure 21 with a norm residual of 1.4%.

The angle is calculated with values from measurements #1 and #8 listed in table 7. The values are assigned,

$$z_2 = 3.50 \cdot 10^{-3} \text{m}, r_2 = 4.76 \cdot 10^{-3} \text{m}, z_1 = 0 \text{ \& } r_1 = 3.90 \cdot 10^{-3} \text{m}$$

With these  $z_{21}$  and  $r_{21}$  are calculated as follows:

$$\begin{aligned} z_{21} &= z_2 - z_1 = 3.50 \cdot 10^{-3} \text{m} \\ r_{21} &= r_2 - r_1 = 0.86 \cdot 10^{-3} \text{m} \end{aligned}$$

The corresponding errors in these values are calculated as follows

$$\begin{aligned} \Delta r_{21} &= \Delta r_2 + \Delta r_1 = 10^{-5} + 10^{-5} = 2 \cdot 10^{-5} \\ \Delta z_{21} &= \Delta z_2 + \Delta z_1 = 10^{-5} + 10^{-5} = 2 \cdot 10^{-5} \end{aligned}$$

The following value is for  $\alpha$  is calculated with the values  $z_{21}$  and  $r_{21}$ :

$$\alpha = \tan^{-1} \left( \frac{r_{21}}{z_{21}} \right) = \tan^{-1} \left( \frac{0.86 \cdot 10^{-3}}{3.50 \cdot 10^{-3}} \right) = 0.25 \text{ rad}$$

The corresponding error in  $\alpha$  is calculated with equation 50 as follows:

$$\begin{aligned} \Delta \alpha &= \left| \frac{z_{21}}{z_{21}^2 + r_{21}^2} \right| \cdot \Delta r_{21} + \left| -\frac{r_{21}}{z_{21}^2 + r_{21}^2} \right| \cdot \Delta z_{21} \\ &= \left| \frac{3.50 \cdot 10^{-3}}{(3.50 \cdot 10^{-3})^2 + (0.86 \cdot 10^{-3})^2} \right| \cdot 2 \cdot 10^{-5} + \left| -\frac{0.86 \cdot 10^{-3}}{(3.50 \cdot 10^{-3})^2 + (0.86 \cdot 10^{-3})^2} \right| \cdot 2 \cdot 10^{-5} \\ \Delta \alpha &= 0.0067 \text{ rad} \approx 0.01 \text{ rad} \end{aligned}$$

The  $NA$  is then calculated with equation 51 as follows:

$$NA = \sin(0.25) \approx 0.25$$

The corresponding error in  $NA$  is calculated is follows:

$$\Delta NA = \sin(\Delta \alpha) = \sin(0.01) \approx 0.01$$

Thus the  $NA$  determined by means of CCD measurements is:

$$NA = 0.25 \pm 0.01$$

The  $NA$  determined means of CCD measurements falls within the error defined in the spectrally measured  $NA$  values, but still diverges with 13% from the manufacturer defined  $NA$ . The cause of this divergence will be discussed in paragraph 7.1.2.

The radius that corresponds to the manufacturer defined  $NA$  at the position defined as  $z = 0$  m is calculated with equation 28 as follows:

The true distance between fiber and CCD element is calculated with equation 28. This gives:

$$z = \frac{r_{average}}{\tan(NA)} = \frac{3.90 \cdot 10^{-3}}{\tan(0.25)} \approx 15.27 \cdot 10^{-3} \text{ m}$$

Then the radius corresponding to the manufacturer defined  $NA$  is calculated with equation 28. This gives:

$$r = \tan(NA) \cdot z = \tan(0.22) \cdot 15.27 \cdot 10^{-3} \approx 3.41 \cdot 10^{-3} \text{ m}$$

An image of the fiber output radiation profile without a pinhole at the fiber proximal end was also taken at point  $z = 0 \text{ m}$  and the profile radius was also determined by means of line profiling.

The CCD images taken of the fiber profile with and without pinhole at the fiber proximal end are illustrated next to each other in figure 22. The corresponding line profiles are shown in figure 23.

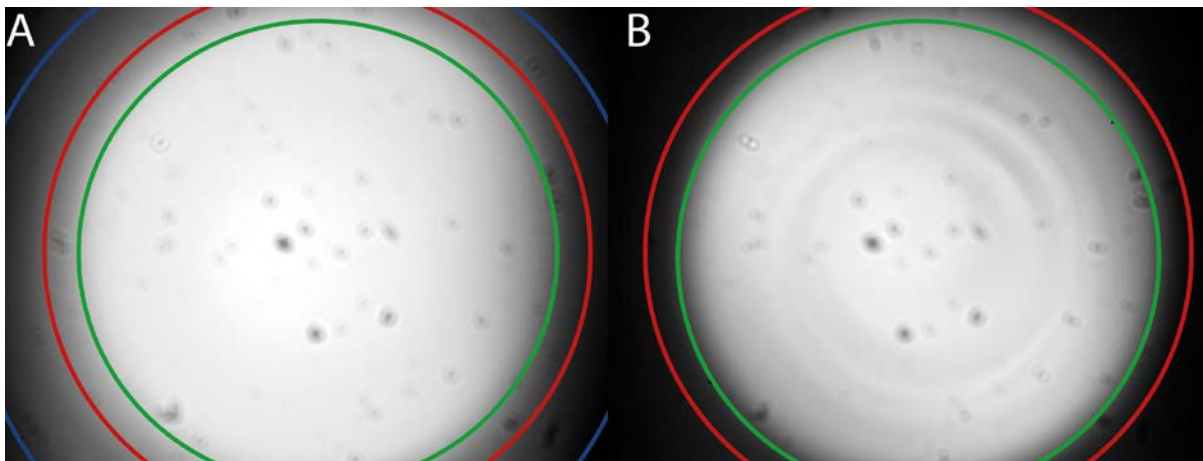


Figure 22: CCD images of output profiles measured from a 200  $\mu\text{m}$  fiber A) without and B) with 100  $\mu\text{m}$  pinhole. The green circles indicate radius corresponding to the manufacturer specified  $NA_{fib}$ . The red circles indicate the  $NA$  measured for a 200  $\mu\text{m}$  fiber with 100  $\mu\text{m}$  pinhole. The blue circle indicates the  $NA$  measured for a 200  $\mu\text{m}$  fiber without 100  $\mu\text{m}$  pinhole.

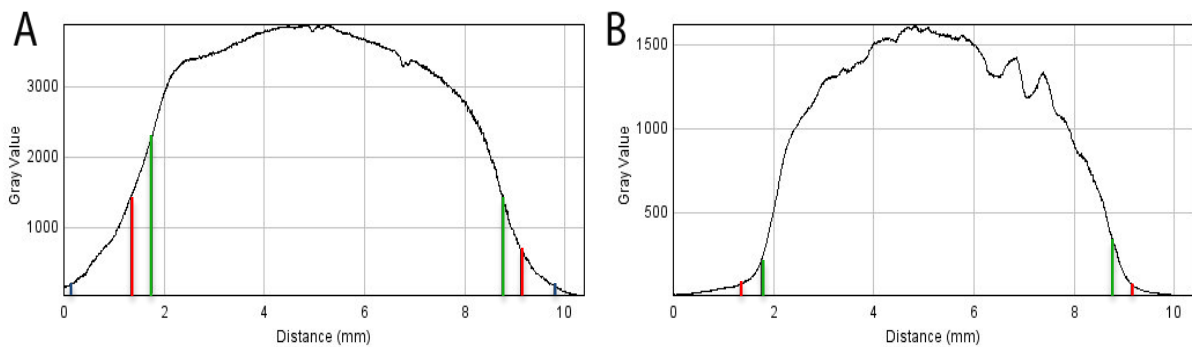


Figure 23: Line profiles of the output profiles from a 200  $\mu\text{m}$  fiber A) without and B) with 100  $\mu\text{m}$  pinhole

Circles that correspond to the manufacturer specified  $NA$ , the  $NA$  calculated from the fiber profile with pinhole and the  $NA$  calculated from the fiber profile without pinhole are drawn on the CCD images. The colored lines in the profiles shown in figure 23 correspond in color with the circles drawn in the CCD images.

The green circle in figure 22B, shows that the bright spot is defined by the manufacturer specified  $NA$ . On the other hand, the red circle that defines the radius determined with line profiling is noticeably larger. This indicates the presence of light that is exiting the fiber at angles larger than the fiber acceptance angle which is the cause of the divergence between the  $NA$  determined with line profiling and the manufacturer defined  $NA$ . The cause of light exiting the fiber at angles larger than the fiber acceptance angle in the presence of a pinhole at the fiber proximal end is explained in Paragraph 7.1.2.

Furthermore, figure 22B also shows the presence of ring patterns inside the spot that is defined by the manufacturer specified  $NA$ . These rings are caused by diffraction effects at the pinhole surface, and are the cause of the two minima seen in the profile shown in figure 24B.

Moreover, figure 23A shows that, in the absence of the pinhole at the fiber proximal end, the fiber output profile is modified by light exiting the fiber at angles larger than the fiber acceptance angle. This is caused by cladding modes. The 5% radius measured for the profile shown in figure 23A is indicated with the blue circle.

The speckles in both CCD images are caused by dust particles on the glass slab in front of the CCD element.

### 6.3 Fiber bending measurements.

The raw spectra, measured at certain angles, for  $d_{fib} \in [200 \ 400 \ 800] \mu\text{m}$  for the smallest bend induced on each fiber are presented in figure 24.

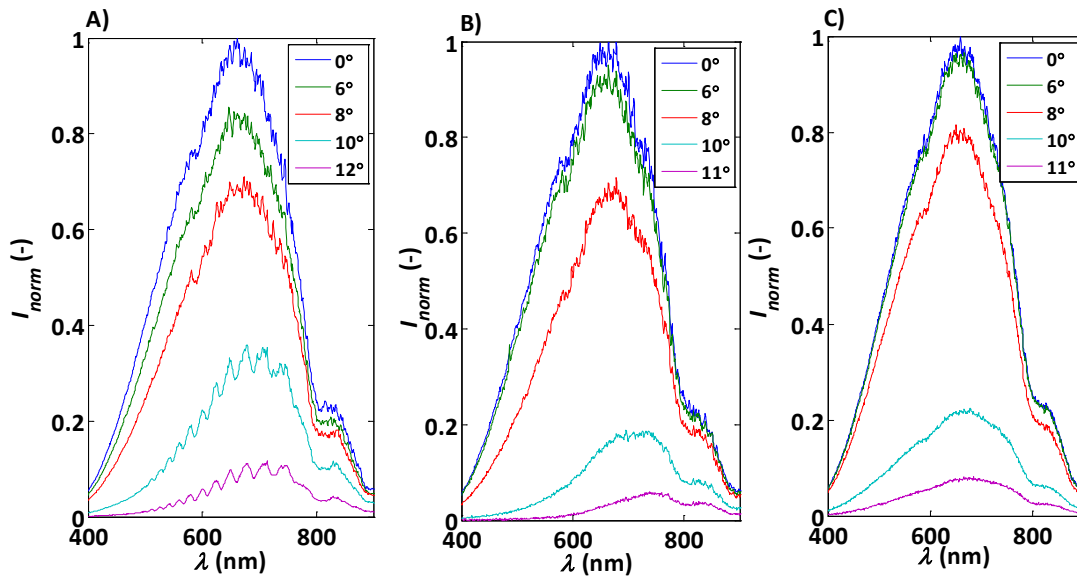


Figure 24: Measured spectrum at certain angles from A) a 200  $\mu\text{m}$  fiber, B) a 400  $\mu\text{m}$  fiber and C) a 800  $\mu\text{m}$  fiber for the smallest bend induced on each fiber. The radii of the bends induced on the 200, 400 and 800  $\mu\text{m}$  fibers were  $8 \cdot 10^{-3} \text{ m}$ ,  $22 \cdot 10^{-3} \text{ m}$  and  $40 \cdot 10^{-3} \text{ m}$  respectively.

Figure 24A, which illustrates the raw spectra measured from a 200  $\mu\text{m}$  fiber, shows the presence of two types of attenuations of light that are both the most visible at larger angles. The first is a larger attenuation of light at lower wavelengths, which can also be seen in in figure 25B, which causes an apparent displacement of the spectra to higher wavelengths. The second is an oscillatory wavelength dependent attenuation which is the most noticeable at higher angle.

Furthermore, it can be seen that the oscillatory wavelength dependent attenuation is absent in figure 24B, which illustrates the raw spectra measured from the 400  $\mu\text{m}$  fiber. It can also be seen that both attenuation mechanisms are absent in figure 24C, which illustrates the raw spectra measured from the 800  $\mu\text{m}$  fiber. These effects are also absent, in all fibers, when larger bends are induced. The reason for the absence of these attenuation effects is discussed in paragraph 7.1.3.

The experimentally extracted and theoretically calculated  $NA_{eff}$  values for the three fibers at different bend radii are presented in figure 25.

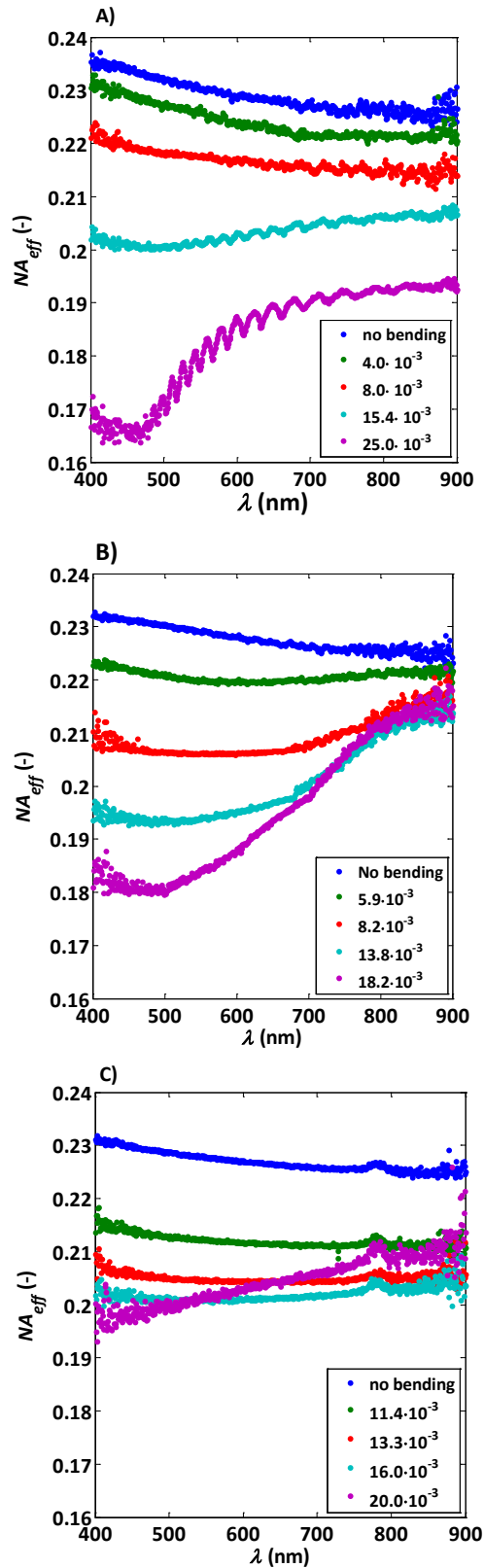


Figure 25: The experimentally extracted  $NA_{eff}$  for A) a 200  $\mu\text{m}$  fiber B) a 400  $\mu\text{m}$  fiber and C) a 800  $\mu\text{m}$  fiber for a range of five arbitrary bend radii per fiber. The error bars are omitted for to conserve figure clarity. The error in the measurements correspond to the errors shown in paragraph 6.1 for the corresponding fibers.

The different colored markers in Figures 26A-F indicate the different bend radii induced per fiber. The bend radii are presented in the ratio of  $d_{fiber} / R_{bend}$  to be able to compare results between measured for different fiber diameters.

The experimentally extracted  $NA_{eff}$  for all three fibers, illustrated in figure 25A, B and C, all show a monotonic decrease with an increase in  $d_{fib}/R_{bend}$ , which corresponds to a decrease in bend radius. In addition, oscillatory patterns are superimposed on the  $NA_{eff}$  slopes when smaller bends are induced on the fibers.

Figure 25A shows the presence of two oscillatory patterns, a fast oscillating pattern and a slow oscillating pattern. It can be seen that the fast oscillating pattern is only present in figure 25A for  $NA_{eff}$  curves measured at small bend radii. The cause of this is discussed in paragraph 7.1.3.

Moreover, a comparison of the experimental results shown in figure 25A with results shown in figure 25C show an increase in the amplitude of the slow oscillating pattern. This is most noticeable when comparing the curves corresponding to  $d_{fib}/R_{bend} = 25.0 \cdot 10^{-3}$  and  $d_{fib}/R_{bend} = 18.2 \cdot 10^{-3}$  shown in figure 25A and Figure 25B, respectively. On the other hand, comparison of figure 25A and figure 25B with figure 25C show a decrease in amplitude of the low oscillating pattern.

Figure 25C shows an increase in  $NA_{eff}$ , at practically all wavelengths, for the  $NA_{eff}$  curve corresponding to the smallest bend radius induced on the fiber. This increase in  $NA_{eff}$  can also be seen in figure 25B between the blue and the violet curves at wavelengths larger than 700 nm. It is clear that the increase in  $NA_{eff}$  seen in figure 25B and C is not caused by bending the fiber, which is expected to decrease the  $NA_{eff}$ . Possible causes for the increase in  $NA_{eff}$  shown in figure 25B and C are discussed in paragraph 7.1.3.

The experimental results illustrated in figure 25C all show a small peak between the wavelengths of 750 and 800 nm. It is clear that the peak that is seen in all measurements is not caused by bending the fiber, because it is also visible when the fiber is not bent. The peaks are also not caused by irregularities on the fiber surface, because the fiber was polished before use. This means that the peaks are caused by background light.

## 7. Discussion & Conclusion

---

### 7.1 Discussion

#### 7.1.1 Fiber NA measurements

Results illustrated in figure 17 and figure 18 show the presence of light exiting the fiber at angles that are larger than the  $\alpha_{max}$  specified by the manufacturer. This light is absent when a pinhole of  $d_{pinhole} > d_{fib}$  is placed at the fiber proximal end. This shows that the cause of light exiting the fiber at higher angles is caused by light that is coupled into the cladding at the fiber proximal end. It can be concluded that cladding modes are the cause.

The result of cladding modes is an experimentally extracted  $NA$  value that diverges by approximately a factor of 2, as can be seen in Figure 19. Figure 19 also shows a difference in extracted  $NA$  values between the 200 and 400  $\mu\text{m}$  fiber for measurements without pinhole at the fiber proximal end. It can be seen that the discrepancy between the  $NA$  values extracted from the 200 and 400  $\mu\text{m}$  fiber is slightly larger than the error calculated for the  $NA$  values. This means that this discrepancy is not caused by experimental error. Examination of the profiles shown in figure 17A and C, at angles near the 5% angle, show an increase of intensity measured of approximately 2% for the 400  $\mu\text{m}$  fiber. This shows that light is slightly less attenuated by the 400  $\mu\text{m}$  fiber. A possible reason for this is a difference in fiber length, which causes a difference in attenuation.

As mentioned previously, pinholes were used to prevent light from directly being coupled in the cladding. Pinhole diameters of  $d_{pinhole} \in [100\ 150] \mu\text{m}$  were used in this study.

Moreover, figure 17B and D show a modification in profile peak when the pinholes are placed in front of the respective fibers. The modification in profile shape is obviously caused by diffraction effects on the pinhole surface. This is most noticeable from the peaks on top of the profile shown in figure 17D, which correspond to an airy disk seen within the profile when measuring.

The effect that diffraction on the pinhole has on the extracted  $NA$  values has been addressed by comparing extracted  $NA$  values from measurements done with different pinhole sizes and fiber diameters, which are the results shown in figure 19. The results shown in figure 19 are all in agreement with the  $NA$  specified by the manufacturer, which shows that the  $NA$  determined experimentally is not effected by diffraction occurring at the pinhole surface.

Fiber/detector separations applied in the measurements were all smaller than the separations calculated with equation 27 in Appendix II. This was primarily because of the low signals measured when applying large fiber/detector separations. As mentioned previously, integration times used varied from 2000 to 10000 ms in order to increase the signal of light measured. The improvement in signal was minimal.

Thus measurements were done for different fiber/detector separations with different fibers to investigate the change in extracted  $NA$  when  $z < z_{FF}$ . A measurement was also done for  $z > z_{FF}$  to compare with measurements done in the  $z < z_{FF}$ . Figure 20 shows the extracted  $NA$  values for measurements done with different  $z$  and  $d_{fib}$ , which are all in agreement with the  $NA$  specified by the manufacturer. Differences are not seen in the  $NA$  extracted from different measurements done with different  $z$ . This is because the manufacturer defined  $NA$  is defined by geometric optics, with rays that exit the fiber at a certain angle. Effects that may have an influence on the measured signal

when measuring at distances that are shorter than the distance calculated in equation 27 are caused by diffractive effects. But because the apertures, which are the  $d_{fib}$  used, are much larger than the wavelengths diffraction effects will only be noticeable at small fiber/detector separations.

### 7.1.2 CCD camera measurements

Measurements were performed with a CCD camera in order to validate the measurements performed spectrally. The measurements were done on a 200  $\mu\text{m}$  which had the shortest calculated distance,  $z_{FF}$ . The measurements resulted in a  $NA = 0.25 \pm 0.01$ , which is larger than the  $NA$  extracted spectrally and the  $NA$  specified by the manufacturer, but still falls within the error calculated spectrally.

The value for the radius corresponding to the manufacturer specified  $NA$  was calculated. A circle defined by that radius and a circle defined by the radius determined from the CCD camera measurements were drawn into the original CCD image. This is shown in figure 22B. Figure 22B shows that the intense spot is defined by the manufacturer defined  $NA$ . This is because the circle corresponding to the manufacturer specified  $NA$  is approximately the same size as the spot.

On the other hand, the circle corresponding to the radius determined with the CCD measurements is noticeably larger. This shows the presence of light exiting the fiber at angles larger than the angles that define the manufacturer specified  $NA$ . It has been shown previously that this is caused by cladding modes, which means that light is being coupled into the cladding. This can only be caused by a misalignment of the fiber proximal end with the pinhole in which a fraction of light is coupled into the cladding.

### 7.1.3 Fiber bending measurements

It is obvious that the oscillatory patterns seen the  $NA_{eff}$  curves for all fiber in figure 25A, B and C are caused by the attenuation mechanisms seen in figure 24.

These oscillatory patterns resemble the results obtained by [13] which are illustrated in figure 12. It was proven by [13] that the oscillatory patterns are caused by interference of light propagating in the core with light propagating in the cladding and/or buffer. Herein, the fast oscillatory pattern is caused by interference between core and buffer light and the slow oscillating pattern is caused by interference between core and cladding light. This means that the attenuation mechanisms and hereby the oscillations seen in  $NA_{eff}$ , seen in the measurement results, are caused by interference between light propagating in the core and light propagating in the cladding and/or buffer.

The absence of the fast oscillating pattern in figure 25B and C is caused by total attenuation of light that is propagated by the buffer. This is a reasonable assumption since the dimensions of the buffers in the 400 and 800  $\mu\text{m}$  fibers are larger than the buffer in the 200  $\mu\text{m}$  fiber. This means that light describes a longer optical path length when propagated by the buffer in the 400 or 800  $\mu\text{m}$  fiber, which results in a larger attenuation of light.

The origin of the increase in amplitude of the slow oscillating pattern seen in figure 25B is not exactly known. A possible cause is the difference in diameter of the pinhole placed at the fiber proximal end, in which more light is coupled into the fiber. This leads to more light being decoupled from the core into the cladding when the fiber is bent and results in a stronger interference of light propagated by the cladding and light propagated by the core. As mentioned before, this is an

assumption and further investigation would have to be done to confirm the validity of this assumption.

The decrease in amplitude of the slow oscillating pattern is most likely caused by a higher attenuation due to an increase in path length described by light propagated by the cladding.

The apparent increase in the  $NA_{eff}$  seen in figure 25B and C are unexpected results because bending a fiber is expected to reduce the  $NA_{eff}$ . This indicates that the increase is not caused by fiber bending. The next obvious cause is experimental error, which is caused by a combination of poor readout resolution of the rotational stage and the extraction method of the wavelength dependent  $NA_{eff}$  with Matlab.

## 7.2 Conclusion

The focus of this study was the characterization of the fiber Numerical Aperture dependence on wavelength and bending of step index multimode optical fibers. This is done to increase accuracy of measurements performed with the SFR technique. Measurements were done with and without pinhole at the fiber proximal end to show the presence of cladding modes and the effect that cladding modes have on the  $NA$  measured. The measurements results prove the presence of cladding modes when no pinhole is placed at the fiber proximal end. The measurement results show an increase of approximately a factor of two when caused by cladding modes. Measurements with pinhole show that diffraction occurs at the pinhole surface, which modifies the peak of the profile measured. Results of measurements done with different fiber diameters and different pinhole diameters show are all in agreement with the  $NA$  specified by the manufacturer. This shows that diffraction effect on the pinhole have no effect on the  $NA$  extracted experimentally. To improve the measured signal, measurements were also done at distances that are shorter than the distance calculated to be in the far field region. These measurements were compared to a measurement done with a 200  $\mu\text{m}$  in the far field. Results show no change in the measured  $NA$ .

The overall results for all measurement with pinhole show a slight decrease in the  $NA$  of 0.23 to 0.22 in a spectral range of  $\lambda \in [400 - 900]$  nm with an uncertainty of 0.02. The curve which is followed by  $NA$  as function of  $\lambda$  is in agreement with results published by [8] and [9].

The CCD camera measurements, performed on a 200  $\mu\text{m}$  fiber with a 100  $\mu\text{m}$  pinhole at the fiber proximal end, resulted in a  $NA \approx 0.25 \pm 0.1$  which shows a slight discrepancy with the manufacturer specified  $NA$ . Plotting circles, which are defined by the calculated  $NA$  and manufacturer specified  $NA$ , in the original CCD image show that the discrepancy in  $NA$  determined by CCD camera measurements was caused by cladding modes. A CCD image taken of the fiber profile without pinhole at the proximal end show the presence of cladding modes as a vague ring of light around the central spot that is defined by the  $NA$ .

Bending of the fibers resulted in a monotonic decrease in  $NA_{eff}$  at large bend radii. When applying small bend radii a wavelength dependent oscillatory relation of the  $NA_{eff}$  consisting of two different oscillation frequencies was seen. The cause of these oscillations were described qualitatively with results published by [13]. Due to lack of time it was not possible to derive an analytical expression to describe bending quantitatively. This is left as a subject of further research.

# Bibliography

---

1. **Jacques, Steven L. and Prah, Scott A.** Introduction to biomedical optics. *Biomedical Optics in Portland*. [Online] Oregon Health & Science University, 2012.  
<http://omlc.ogi.edu/education/ece532/class3/index.html>.
2. *Measurement of the reduced scattering coefficient of turbid media using single fiber reflectance spectroscopy: fiber diameter and phase function dependence.* **Kanick, S.C, et al., et al.** 1, Rotterdam : Biomedical Optics Express, 20110, Vol. 2. 1687-1702.
3. *Method to quantitatively estimate wavelength-dependent scattering properties from multidiameter single fiber reflectance spectra measured in a turbid medium.* **Kanick, S.C., et al., et al.** 15, Rotterdam : Optics Letters, 2011, Vol. 36. 2997.
4. *Collection efficiency of a single optical fiber in turbid media.* **Bargo, P.R., Prah, S.A. and Jacques, S.L.** 16, Oregon : Applied Optics, 2003, Vol. 42. 3187-3197.
5. **Kasap, S.O.** *Optoelectronics and photonics*. New Jersey : Prentice Hall, 2001. 64.
6. **Hecht, Eugene.** *Optics*. Sansome St. San Francisco : Addison Wesley, 2002. 122-124.
7. —. *Optics*. Sansome St., San Francisco : Addison Wesley, 2002. 67-72.
8. *Refractive index dispersion and related properties in fluorine doped silica.* **Wood, J.W. Fleming and D.L.** 19, Murray Hill, New Jersey : Applied optics, 1983, Vol. 22.
9. *Measurement of fiber profile dispersion in optical fibres: A direct technique.* **Sladen, F.M.E, Payne, D.N. and Adams, M.J.** 7, Southampton, England : Electronic Letters, 1977, Vol. 13. 212-213.
10. *Data distribution using fiber optics.* **Barnoski, M.K.** 11, Malibu, California : Applied Optics, 1975, Vol. 14. 2571-2577.
11. *Effect of cladding modes on the far-field radiation pattern for a multimode step-index optical fiber.* **Payne, Richard and Bouthillette, O.,Lionel.** 14, Massachusetts : Applied Optics, 1978, Vol. 17. 2132-2134.
12. *Bending loss in multimode fibers with graded and ungraded core index.* **Gloge, D.** 11, New Jersey, U.S. : Applied Optics, 1972, Vol. 11. 2506-2509.
13. *Observation of secondary bend loss oscillations arising from propagation of cladding modes in buffered monomode optical fibres.* **Morgan, R., et al., et al.** 1, Edinburgh, UK : Optics communications, 1991, Vol. 85. 17-20.
14. **Hecht, Eugene.** *Optics*. Sansome St., San Francisco : Addison Wesley, 2002. 447-449.
15. —. *Optics*. Sansome St., San Francisco : Addison Wesley, 2002. 444.



## Appendix I: Internship assignment

---

Optical fibers are often used in diagnostic measurements that are done with light. In the Erasmus MC, single fibers are used for the delivery of light to tissue as well as the collection of reflected light, which is analyzed with a spectrograph. The mathematical models to analyze SFR use the fiber Numerical Aperture,  $NA$ , as input parameter. However, the  $NA$  is not well characterized and leads to an unknown error in the tissue measurements. Therefore, a number of factors have to be investigated to better characterize the accuracy of the measurements and, if needed, develop calibration methods to minimize the dependence of the  $NA$ . Specifically, we want to know the dependence of effective  $NA$  on fiber length, fiber bending and launch conditions, and how we can correct for these factors.

# Appendix II: Calculations

## II.1 Far field distance calculations

The fiber diameters used are  $d_{fib} \in [200 \ 400 \ 800] \cdot 10^{-6}$  m and the distance of the far field region for each  $d_{fib}$  is calculated with equation 27.

An example calculation is given by taking the fiber diameter  $d_{fib} = 200 \cdot 10^{-6}$  m and the smallest measured wavelength,  $\lambda = 400 \cdot 10^{-9}$  m. This results in a distance,

$$z_{FF} > \frac{d_{fib}^2}{\lambda} = \frac{(200 \cdot 10^{-6})^2}{400 \cdot 10^{-9}} = 0.1 \text{ m}$$

Where:

$z_{FF}$  : The theoretically defined Far Field distance [m]

The calculated distance for the other measurement fibers are listed in table 8.

Table 8: Calculated distance of the far field region for various  $d_{fib}$  with  $\lambda = 400 \cdot 10^{-9}$  m

$d_{fib}$ ( $10^{-6}$ m)	$z_{FF}$ (m)
200	0.1
400	0.4
800	1.6
1000	2.5

## II.2 Axial alignment error

The error,  $\alpha_{axerr}$ , in the measured angle due to misalignment of the fiber with the rotational stage axis is derived as follows:

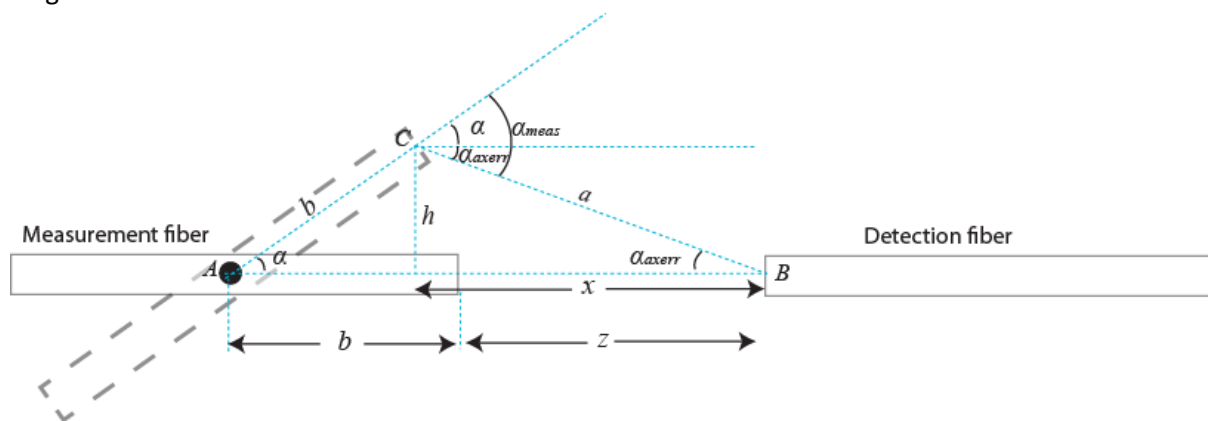


Figure 26: Fiber axial positioning error.

It can be derived from figure 26 that when the fiber output is misaligned with the rotational stage axis, the measured angle is described by the following expression,

$$\alpha_{meas} = \alpha + \alpha_{axerr} \quad (29)$$

Where:

$\alpha_{meas}$	: The true angle measured	[rad]
$\alpha$	: The chosen measurement angle	[rad]
$\alpha_{axerr}$	: The error in the measurement angle	[rad]

The following expression is obtained when applying the sine law to triangle ABC,

$$\frac{\sin(\alpha)}{a} = \frac{\sin(\alpha_{axerr})}{b} \quad (30)$$

It can be seen in the figure that,

$$a = \sqrt{x^2 + h^2} \quad (31)$$

$$x = (b + z) - b \cdot \cos(\alpha) \quad (32)$$

$$h = b \cdot \sin(\alpha) \quad (33)$$

Where:

$b$	: The offset of with the rotational stage axis	[m]
$x$	: The distance between detection fiber and rotational stage axis	[m]
$h$	: Lateral displacement due to axial offset	[m]
$a$	: The distance between fiber core centers	[m]

By substituting equations 32 and 33 into equation 31 the following expression is obtained:

$$a = \sqrt{((b + x) - b \cdot \cos(\alpha))^2 + (b \cdot \sin(\alpha))^2}$$

This is equivalent to:

$$a = \sqrt{(b \cdot \cos(\alpha))^2 + (b + x)^2 - (2 \cdot (b + x) \cdot b \cdot \cos(\alpha)) + (b \cdot \sin(\alpha))^2} \quad (34)$$

By substituting the following equations,

$$(b \cdot \cos(\alpha))^2 = b^2 \cdot \cos(\alpha)^2$$

$$(b \cdot \sin(\alpha))^2 = b^2 \cdot \sin(\alpha)^2$$

$$\sin(\alpha)^2 + \cos(\alpha)^2 = 1$$

into equation 34, the following is obtained:

$$a = \sqrt{b^2 + (b + z)^2 - (2 \cdot (b + z) \cdot b \cdot \cos(\alpha))} \quad (35)$$

Substitution of equation 35 into equation 30 gives,

$$\frac{\sin(\alpha)}{\sqrt{b^2 + (b + z)^2 - (2 \cdot (b + z) \cdot b \cdot \cos(\alpha))}} = \frac{\sin(\beta)}{b} \quad (36)$$

and rearrangement of equation 36 gives the following:

$$\sin(\alpha_{axerr}) = \frac{b \cdot \sin(\alpha)}{\sqrt{b^2 + (b + z)^2 - (2 \cdot (b + z) \cdot b \cdot \cos(\alpha))}} \quad (37)$$

Finally, by applying the inverse sine to equation 37 gives the following:

$$\alpha_{axerr} = \sin^{-1} \left( \frac{b \cdot \sin(\alpha)}{\sqrt{b^2 + (b + z)^2 - (2 \cdot (b + z) \cdot b \cdot \cos(\alpha))}} \right) \quad (38)$$

The error in the measured angle due to fiber misalignment with the rotational stage axis can be calculated with equation 38. The corresponding error in the measured  $NA$  can be calculated with equation 39.

$$NA_{axerr} = n_0 \sin(\alpha_{axerr}) \quad (39)$$

Where:

$NA_{axerr}$  : The offset in the measured  $NA$  due to axial misalignment [-]

Since the extent of the misalignment with the rotational stage axis is unknown, it will be assumed that  $b = 1$  mm. Also,  $\alpha_{axerr}$  will be calculated from the average Numerical Aperture,  $NA_{average}$ .

Hereby an example calculation with values from the 200  $\mu$ m fiber 100  $\mu$ m pinhole measurement, presented in figure 18:

$$b = \pm 10^{-3} \text{ m}, x = 7 \cdot 10^{-2} \text{ m} \ \& \ NA_{average} = 0.22 \rightarrow \alpha \approx 0.22 \text{ rad}$$

$\alpha_{axerr}$  is calculated as follows:

$$\alpha_{axerr} = \sin^{-1} \left( \frac{(10^{-3}) \cdot \sin(0.22)}{\sqrt{(10^{-3})^2 + (10^{-3} + 7.0 \cdot 10^{-2})^2 - (2 \cdot (10^{-3} + 7.0 \cdot 10^{-2}) \cdot (10^{-3} + 7.0 \cdot 10^{-2}) \cdot \cos(0.22))}} \right)$$

$$\alpha_{axerr} \approx \pm 3.2 \cdot 10^{-3} \text{ rad}$$

The following error in  $NA$  is calculated with equation 39:

$$NA_{axerr} = \sin(3.2 \cdot 10^{-3}) \approx \pm 3.2 \cdot 10^{-3}$$

The error,  $\alpha_{axerr}$ , in the measured angle is a systematical error and will not be incorporated in the measurement error bars but will be calculated and listed in separately.

### II.3 Vertical alignment error

An expression for the possible error in measured acceptance angle due to vertical profile alignment errors,  $\alpha_{verterr}$ , is derived as follows:

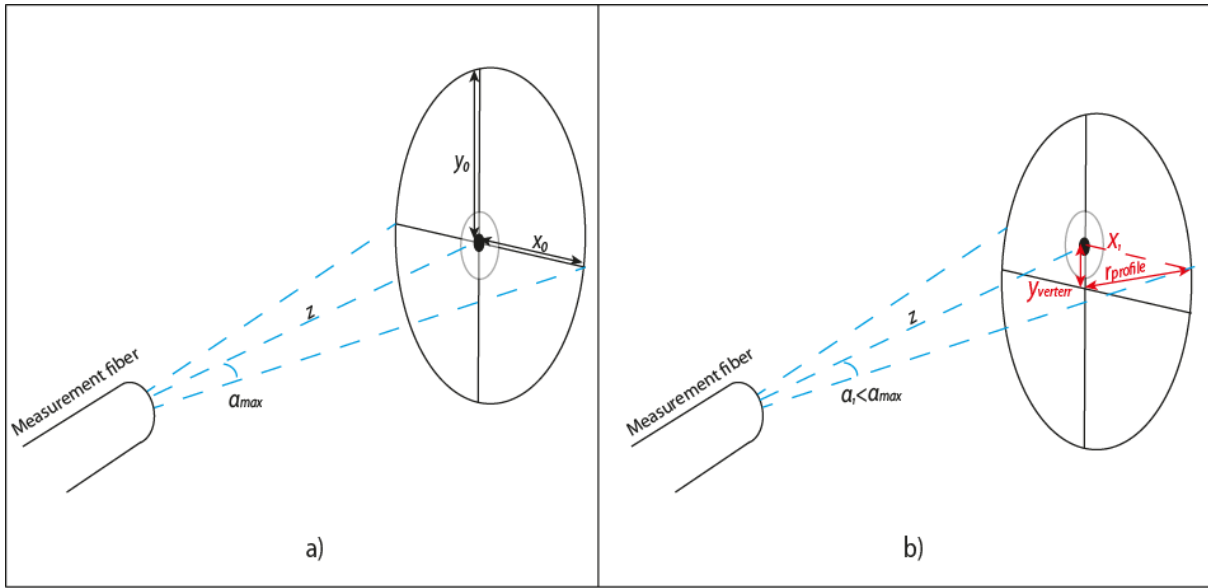


Figure 27: Schematically illustrated a) Vertically aligned profile and b) Vertically misaligned profile.

It can be seen in figure 27 that the fiber acceptance angle is described by the following expression,

$$\tan(\alpha_{max}) = \frac{x_0}{z} = \frac{y_0}{z} \quad (40)$$

Where:

$x_0$  : The profile radius [m]

$y_0$  : The profile radius [m]

$z$  : The distance between measurement fiber and detection fiber [m]

The measured acceptance angle due to vertical profile misalignment is given by the following expression,

$$\tan(\alpha_1) = \frac{x_1}{z} \quad (41)$$

Where:

$\alpha_1$  : The measured acceptance angle due to vertical misalignment [rad]

$x_1$  : The measured profile radius due to vertical misalignment [m]

It can also be seen in figure 27 that,

$$y_{verterr} = \sqrt{(r_{profile})^2 - x_1^2} \quad (42)$$

Where:

$y_{verterr}$  : The vertical of the detection fiber with the profile [m]

Because the pattern is circular the following is true:

$$y_0 = x_0 = r_{profile} \quad (43)$$

Substituting equations 40,41 and 43 into equations 42 results in the following equation,

$$y_{verterr} = \sqrt{z^2 \tan(\alpha_{max})^2 - z^2 \tan(\alpha_1)^2} \quad (44)$$

Reorganization of equation 44 gives the following equation:

$$\tan(\alpha_{max}) - \tan(\alpha_1) = \sqrt{\frac{(y_{verterr})^2}{z^2}} \quad (45)$$

Furthermore, it is known that,

$$\tan(p \pm q) = \frac{\tan(p) \pm \tan(q)}{1 \mp \tan(p) \tan(q)} \quad (46)$$

Application of equation 46 to equation 45 gives the following:

$$\tan(\alpha_{max}) - \tan(\alpha_1) = \tan(\alpha_{max} - \alpha_1) (1 + \tan(\alpha_{max}) \tan(\alpha_1)) = \sqrt{\frac{y_1^2}{z^2}}$$

Reorganization of the above equation gives,

$$\tan(\alpha_{max} - \alpha_1) = \frac{\sqrt{\frac{(y_{verterr})^2}{z^2}}}{(1 + \tan(\alpha_{max}) \tan(\alpha_1))} \quad (47)$$

Because the angles are considered to be moderately small and the differences in the measured acceptance angle are expected to be small, the following approximation can be made:

$$(1 + \tan(\alpha_{max}) \tan(\alpha_1)) \approx 1$$

Applying the above to equation 47 gives:

$$\tan(\alpha_{max} - \alpha_1) = \sqrt{\frac{(y_{verterr})^2}{z^2}}$$

Finally, applying the inverse tangent on the above gives,

$$\alpha_{max} - \alpha_1 = \alpha_{vertterr} = \tan^{-1} \left( \sqrt{\frac{(y_{vertterr})^2}{z^2}} \right) = \tan^{-1} \left( \frac{y_{vertterr}}{z} \right) \quad (48)$$

The error in the measured angle due to detection fiber misalignment with radiation profile be calculated with equation 48 .The corresponding error in the measured  $NA$  can be calculated with equation 49.

$$NA_{vertterr} = n_0 \sin(\alpha_{vertterr}) \quad (49)$$

Where:

$NA_{vertterr}$  : The offset in the measured  $NA$  due to vertical misalignment [-]

Since the extent of the profile misalignment is unknown and because the profile is realigned with the detection fiber after every change , it will be assumed that  $y_{vertterr}$  is at most 10% of  $y_0$ .

Hereby an example calculation with values from the 200  $\mu\text{m}$  fiber 100  $\mu\text{m}$  pinhole measurement, presented in figure 18:

$$x = 7.0 \cdot 10^{-2} \text{ m} \ \& \ NA_{average} = 0.22 \rightarrow \alpha_{max} \approx 0.22 \text{ rad}$$

The profile radius,  $y_0$ , is calculated with equation 40 as follows,

$$y_0 = \tan(\alpha_{max}) \cdot z = \tan(0.22) \cdot 7.0 \cdot 10^{-2} = 1.6 \cdot 10^{-2} \text{ m}$$

and,

$$y_{vertterr} = 0.1 \cdot y_0 = 0.1 \cdot 1.6 \cdot 10^{-2} = 1.6 \cdot 10^{-3} \text{ m}$$

The error in angle caused by profile misalignment is calculated with equation 48 as follows,

$$\alpha_{vertterr} = \tan^{-1} \left( \frac{y_{vertterr}}{z} \right) = \tan^{-1} \left( \frac{1.6 \cdot 10^{-3}}{7.0 \cdot 10^{-2}} \right) \approx 0.023 \text{ rad}$$

The following error in  $NA$  is calculated with equation 49:

$$NA_{vertterr} = \sin(0.023) \approx 0.023$$

Which is,

$$\frac{0.023}{0.22} \cdot 100 = 10\%$$

Since  $y_{vertterr}$  leads to an underestimation of  $NA$ ,

$$NA_{vertterr} = -0.023$$

$y_{verterr}$  is a systematical error and will not be added to the measurement error bars but is shown separately.

## II.4 Acceptance angle and NA error in CCD camera measurements

The error in the angle, calculated from results obtained when doing measurements with the CCD camera, is derived, by means of equation 28, as follows:

$$\Delta\alpha = \left| \frac{\partial\alpha}{\partial r_{21}} \right| \cdot \Delta r_{12} + \left| \frac{\partial\alpha}{\partial z_{21}} \right| \cdot \Delta z_{21} = \left| \frac{1}{1 + \left(\frac{r_{21}}{z_{21}}\right)^2} \cdot \frac{1}{z_{21}} \right| \cdot \Delta r_{21} + \left| \frac{1}{1 + \left(\frac{r_{21}}{z_{21}}\right)^2} \cdot -\frac{r_{21}}{z_{21}^2} \right| \cdot \Delta z_{21}$$

This can be reduced to,

$$\Delta\alpha = \left| \frac{z_{21}}{z_{21}^2 + r_{21}^2} \right| \cdot \Delta r_{21} + \left| -\frac{r_{21}}{z_{21}^2 + r_{21}^2} \right| \cdot \Delta z_{21} \quad (50)$$

The error in NA is calculated with the following equation:

$$\Delta NA = \sin(\Delta\alpha) \quad (51)$$

# Appendix III: The pinhole setup

The pinhole setup that is placed at the measurement fiber proximal end, to prevent cladding modes, is illustrated in figure 28.

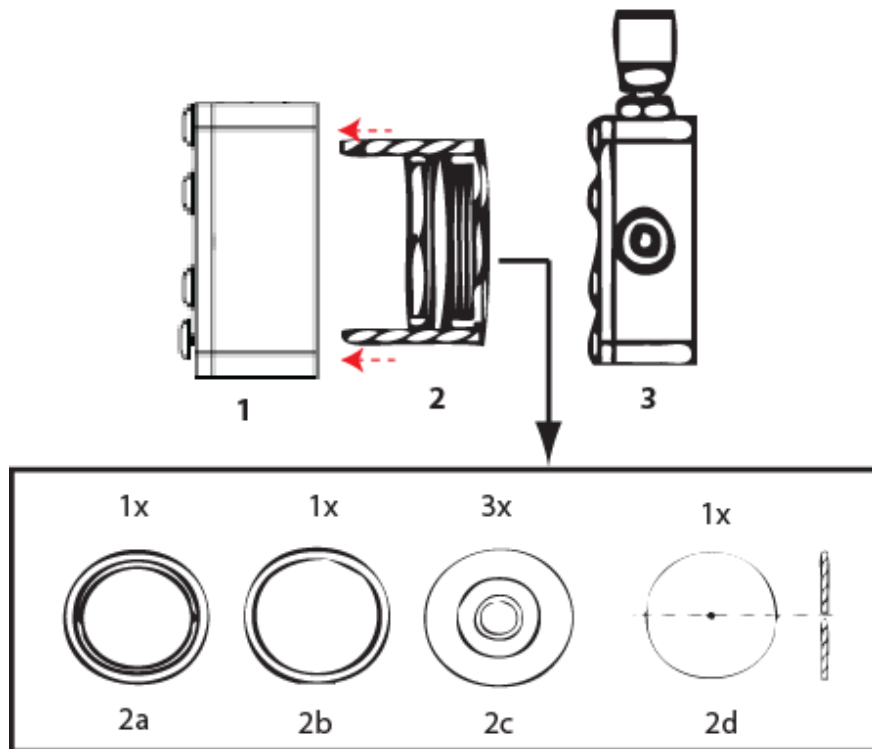


Figure 28: A schematic of the pinhole setup.

The components that are used to build up the pinhole setup are listed in table 9.

Table 9: List of components used to make the pinhole setup.

#	Components	Specifications	
1	<b>Optic mount</b>	–	–
2	<b>Lens tube</b>	–	–
2a & b	<b>Retaining ring</b>	$\phi$	18 mm
2c	<b>Pinhole carrier</b>	–	–
2d	<b>Pinhole</b>	$t$	0.013 mm
3	<b>x-y translational optic mount.</b>	–	–

The pinhole holder is constructed by placing the components illustrated in figure 28 in order of 2d-a in the lens tube. The pinhole holder is then placed into an optical mount.

Furthermore, the fiber is paced into an x-y translational optic mount in order to be able to align the fiber with the pinhole. The optic mounts containing pinhole holder and fiber are then incorporated into an optical cage system in order to ensure system stability.

Finally, the maximum angle of light that is incident on the pinhole is calculated with the following expression:

$$\tan^{-1}\left(\frac{r_{ring}}{z_{tube}}\right) = \alpha_{pinhole} \quad (52)$$

Where:

- $r_{ring}$  : The inner radius of the retaining ring [mm]  
 $z_{tube}$  : The depth between retaining ring and pinhole [mm]  
 $\alpha_{pinhole}$  : The maximum angle of light incident on the pinhole [rad]

The Numerical Aperture of the pinhole holder is then calculated is follows:

$$NA_{pinhole} = \sin(\alpha_{pinhole})$$

Where:

- $NA_{pinhole}$  : The Numerical Aperture of the pinhole holder [-]

The inner radius of the retaining ring and the depth between retaining ring and pinhole where measured, which resulted in  $z_{tube} = 9.0$  mm and  $r_{ring} = 9.0$  mm.

The following value for  $\alpha_{pinhole}$  is obtained by filling in the values in equation 52,

$$\tan^{-1}\left(\frac{9.0}{9.0}\right) \approx 0.79 \text{ rad}$$

$NA_{pinhole}$  is calculated with equation 53 as follows:

$$NA_{pinhole} = \sin(0.79) \approx 0.71$$

By comparing the  $NA_{pinhole} = 0.71$  with the expected  $NA = 0.22$ , it is obvious that  $NA_{pinhole}$  is more than enough to fulfill the requirement for angularly overfilling the fiber.